

# Resistivity of Single Crystal Molybdenum Dioxide

Kurtis Bauer

Condensed Matter Physics and Materials Science

Submitted in partial fulfillment  
of the requirements for the degree of

M.Sc. Physics

Faculty of Mathematics and Science, Brock University  
St. Catharines, Ontario

© 2020

# Abstract

The chemical vapour transport method was used to grow molybdenum oxide single crystals so that their electrical properties could be analyzed. Satisfactory single crystal samples of  $\text{MoO}_2$  and  $\text{Mo}_4\text{O}_{11}$  were grown successfully using  $\text{I}_2$  as a transport agent. Crystal growths using  $\text{TeCl}_4$  as a transport agent were also performed, though with mixed results. This approach yielded  $\text{MoO}_2$ ,  $\text{MoO}_3$ , and  $\text{Mo}_9\text{O}_{26}$ , but this produced samples of a quality not suitable for single crystal analysis. Measurements performed on these samples yielded unique results, due to their mixed oxide nature, but as the composition of each sample was inconsistent, even between crystals from the same growth, little can be said about them definitively. Rubidium doped single crystal growths were also attempted, to build on previous polycrystalline Rb doped sample research, however no growths successfully included measurable amounts of Rb. While resistivity and heat capacity measurements performed on  $\text{MoO}_2$  did identify a phase transition in the area of 267K reported by other researchers, there was however no evidence found to support a reported 220K electronic transition [1]. In  $\text{Mo}_4\text{O}_{11}$  two previously identified 109K and 30K charge density wave transitions were observed in the DC resistivity. When AC resistivity measurements were performed the 30K transition was not apparent. Instead, a divergence of the cooling and warming curves not seen in the DC experiments occurred above 200K, with previously unseen peaks appearing at 285K and 250K when cooling from 400K.

# Acknowledgements

First and foremost I thank Dr. Fereidoon Razavi, without his direction and support none of this would have been possible. As my supervisor he has given me an amazing opportunity to improve myself, as both a scientist and as a person, it has been an experience which I will never forget. I also thank my committee members Dr. Maureen Reedyk and Dr. Thad Harroun for helping to guide me through my research, courses, and all other aspects of this program.

I thank my parents and siblings, for making sure that I had the time I needed to complete my work, while also helping me to find balance between my studies and the many other important things in life. They made this goal attainable and throughout it all have made my life enjoyable.

Along with the rest of my family, I owe my grandparents a special thanks for their unshakeable faith in my ability to succeed. Their encouragement played a huge part in my decision to pursue this degree.

Finally, all of my classmates and colleges. Their assistance throughout my many years of schooling has been indispensable. Whether it was giving help with difficult courses, insight into unfamiliar topics, or guidance in the lab, without them all of these things would have been that much harder. In particular I would like to thank my dear friend Jesse, for his invaluable assistance, proof reading, and sanity checking throughout this endeavor.

# Contents

Abstract	i
Acknowledgements	ii
Contents	iii
List of Figures	v
List of Tables	vii
<b>1 Introduction</b>	<b>1</b>
1.1 Transition Metal Oxides . . . . .	1
1.2 Molybdenum Dioxide - $\text{MoO}_2$ . . . . .	3
1.3 Molybdenum Oxide - $\text{Mo}_4\text{O}_{11}$ . . . . .	5
1.4 Low Dimensional Materials . . . . .	7
1.5 Charge Density Waves . . . . .	8
1.6 Chemical Vapour Transport . . . . .	8
1.7 Four Probe Resistivity . . . . .	10
1.8 Objectives . . . . .	12
1.8.1 Sample Preparation . . . . .	12
1.8.2 Resistivity . . . . .	12
1.8.3 Heat Capacity . . . . .	12
1.8.4 Temperature dependent X-Ray Diffraction . . . . .	13
<b>2 Methods</b>	<b>14</b>
2.1 Crystal Growth . . . . .	14
2.2 X-Ray Diffraction . . . . .	18

2.2.1	Powder Diffraction . . . . .	18
2.2.2	Single Crystal Diffraction . . . . .	19
2.2.3	Temperature Control . . . . .	19
2.3	Resistivity Measurements . . . . .	23
2.3.1	Direct Current Resistivity Measurements . . . . .	23
2.4	Heat Capacity . . . . .	24
<b>3</b>	<b>Results</b>	<b>27</b>
3.1	X-Ray Diffraction . . . . .	27
3.1.1	Powder Diffraction - Identification . . . . .	27
3.1.2	Single Crystal Diffraction - Orientation . . . . .	32
3.2	MoO <sub>2</sub> . . . . .	35
3.2.1	Iodine Transport Growth . . . . .	35
3.2.2	Anomalous Peak . . . . .	40
3.3	TeCl <sub>4</sub> Growth . . . . .	46
3.4	Mo <sub>4</sub> O <sub>11</sub> . . . . .	47
<b>4</b>	<b>Discussion and Conclusion</b>	<b>54</b>
4.1	Crystal Growth and Transport Ions . . . . .	54
4.2	MoO <sub>2</sub> Features and Transitions . . . . .	55
4.3	Mo <sub>4</sub> O <sub>11</sub> . . . . .	56
	<b>References</b>	<b>57</b>
<b>A</b>	<b>Appendix</b>	<b>61</b>

# List of Figures

1	MoO <sub>2</sub> Structure . . . . .	3
2	MoO <sub>2</sub> Unit Cell . . . . .	4
3	MoO <sub>2</sub> Octehedra . . . . .	4
4	Chemical Vapour Transport . . . . .	9
5	Linear Four Probe Setup . . . . .	10
6	Van der Pauw Setup . . . . .	11
7	Three Zone Furnace . . . . .	15
8	Unopened Ampule . . . . .	16
9	MoO <sub>2</sub> Crystals from TeCl <sub>4</sub> Growth . . . . .	18
10	Peltier Coolers . . . . .	20
11	Finned Heat Sink In Housing . . . . .	21
12	Frozen Sample Platform . . . . .	22
13	Frozen Heat Sink . . . . .	23
14	Cryostat Sample Mount . . . . .	24
15	Heat Capacity Sample Mount . . . . .	25
16	MoO <sub>2</sub> Powder Diffraction . . . . .	30
17	Mo <sub>4</sub> O <sub>11</sub> Powder Diffraction . . . . .	31
18	Single Crystal and Powder Diffraction MoO <sub>2</sub> . . . . .	32
19	Single Crystal and Powder Diffraction Mo <sub>4</sub> O <sub>11</sub> . . . . .	33
20	AC Resistivity of MoO <sub>2</sub> . . . . .	35
21	Resistivity of MoO <sub>2</sub> Around 220K . . . . .	36
22	Resistivity of MoO <sub>2</sub> Around 267K . . . . .	37
23	Derivative of Resistivity of MoO <sub>2</sub> . . . . .	38
24	Heat Capacity of MoO <sub>2</sub> from 300-200K . . . . .	39

25	MoO <sub>2</sub> Anomalous Peak . . . . .	40
26	MoO <sub>2</sub> Anomalous Peak Suppressed . . . . .	41
27	DC resistivity of MoO <sub>2</sub> . . . . .	42
28	Heat capacity of MoO <sub>2</sub> From 150K to 10K . . . . .	43
29	Resistivity of MoO <sub>2</sub> at 1000Hz . . . . .	44
30	Resistance of copper at 10Hz and 1000Hz . . . . .	45
31	AC Resistivity of MoO <sub>x</sub> Compound TeCl <sub>4</sub> Growth . . . . .	46
32	Crystal thought to be Mo <sub>4</sub> O <sub>11</sub> . . . . .	47
33	DC Resistivity of Mo <sub>4</sub> O <sub>11</sub> . . . . .	48
34	Derivative of DC Resistivity of Mo <sub>4</sub> O <sub>11</sub> . . . . .	49
35	DC Resistivity of Mo <sub>4</sub> O <sub>11</sub> Below 50K . . . . .	50
36	AC Resistivity of Mo <sub>4</sub> O <sub>11</sub> . . . . .	51
37	Derivative of AC Resistivity of Mo <sub>4</sub> O <sub>11</sub> . . . . .	52
38	Heat Capacity of Mo <sub>4</sub> O <sub>11</sub> . . . . .	53

# List of Tables

1.1	MoO <sub>2</sub> Unit Cell . . . . .	3
1.2	$\eta$ -Mo <sub>4</sub> O <sub>11</sub> Unit Cell . . . . .	6
1.3	$\gamma$ -Mo <sub>4</sub> O <sub>11</sub> Unit Cell . . . . .	6
2.1	Growth Temperature Profile . . . . .	15
2.2	MoO <sub>2</sub> Crystals from I <sub>2</sub> Growth . . . . .	16
3.1	I <sub>2</sub> Grown MoO <sub>2</sub> Unit Cell Parameters . . . . .	27
3.2	I <sub>2</sub> Grown Mo <sub>4</sub> O <sub>11</sub> Unit Cell Parameters . . . . .	28
3.3	TeCl <sub>4</sub> Grown Mo <sub>9</sub> O <sub>26</sub> Unit Cell Parameters 1 . . . . .	28
3.4	TeCl <sub>4</sub> Grown Mo <sub>9</sub> O <sub>26</sub> Unit Cell Parameters 2 . . . . .	29
A.1	MoO <sub>2</sub> Diffraction Peak List . . . . .	61
A.2	Mo <sub>4</sub> O <sub>11</sub> Diffraction Peak List . . . . .	66



# 1 Introduction

The objective of this thesis is the examination of the electronic properties of molybdenum oxides, specifically  $\text{MoO}_2$  single crystals grown using the chemical vapour transport (CVT) method. Of particular interest is the resistivity of  $\text{MoO}_2$ , and the examination of possible phase transitions. Identification and analysis of these transitions will be assisted by heat capacity measurements. Due to the unexpected formation of  $\text{Mo}_4\text{O}_{11}$  crystals in some of the  $\text{MoO}_2$  growths, an opportunity to study this material was presented. The examination of  $\text{Mo}_4\text{O}_{11}$  was performed in the same manner as that of  $\text{MoO}_2$ . However special attention was paid to the apparent metal-insulator transition of  $\text{Mo}_4\text{O}_{11}$  at 109K and the potential for charge density wave formation. Single crystal samples were produced using CVT with various combinations of temperatures and transport ions. Due to the variety of possible molybdenum oxides, the chemical composition of samples as verified using x-ray powder diffraction. Single crystal diffraction was also necessary to identify the crystallographic planes of the single crystals, due to the highly anisotropic nature of the materials being studied.

## 1.1 Transition Metal Oxides

Varying definitions exist regarding which elements qualify as transition metals, with groups 4-11 on the periodic table generally being accepted along with some group 3 elements and occasionally group 12 elements. Given the focus of this paper on electronic properties the classification will be limited to elements with a partially filled d valence shell [2]. In their elemental state these partially filled d shells result in materials with low energy gaps and a wide range of stable oxidation states. This range of oxidation states can have a variety of effects on the conductivity of chemically similar materials because the small changes in chemical composition can significantly increase the availability of conduction electrons [3].

The chemical formula of these materials can be complex and the average oxidation state may be non-integer. The metal ions in these materials must be described by either fractional oxidation states or a combination of integer oxidation states [4]. One material is  $\text{Mo}_4\text{O}_{11}$ , which could be viewed, for example, as a 3:1 ratio of  $\text{Mo}^{3+}$  and  $\text{Mo}^{2+}$  ions or as  $\text{Mo}^{2.75+}$ , among other possible combinations. It can be difficult to determine which method of assigning oxidation states to ions in such a material is appropriate. Sometimes the properties of the bulk material are better explained by one approach or the other. For example, fractional oxidation states can imply a greater degree of electron mobility and would thus be more appropriate for highly conductive metal oxides. Insulators on the other hand, lack mobile conduction electrons, therefore, localized electrons with a mixture of integer oxidation states are more fitting. Even in materials with simple stoichiometry, atoms may have complicated oxidation states. These variations in oxidation state and electron availability are part of what make the various molybdenum oxides so interesting and why small oxygen deficiencies can radically alter their electrical properties.

## 1.2 Molybdenum Dioxide - $\text{MoO}_2$

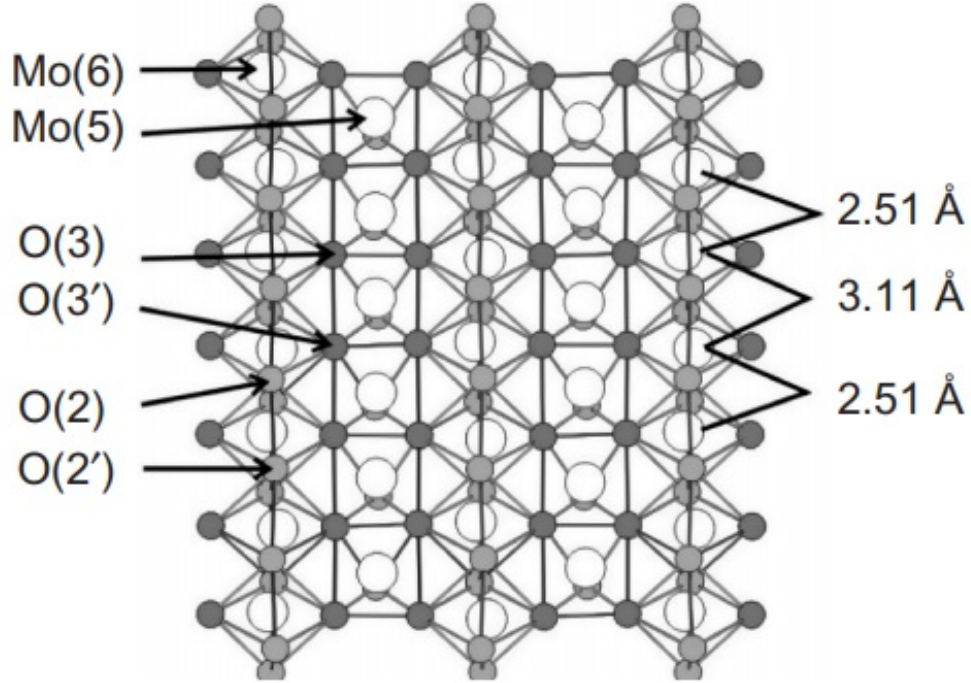


Figure 1:  $\text{MoO}_2$  structure as seen looking into the (011) plane [5].

Molybdenum Dioxide ( $\text{MoO}_2$ ) is a monoclinic molybdenum oxide with a distorted rutile ( $\text{TiO}_2$ ) crystal structure. Unit cell parameters vary slightly between sources, but a typical set of dimensions can be seen in the table below.

Dimension	Length/Angle	Error
a	5.6109Å	$\pm 0.0008\text{\AA}$
b	4.8562Å	$\pm 0.0006\text{\AA}$
c	5.6285Å	$\pm 0.0007\text{\AA}$
$\alpha$	90°	
$\beta$	120.95°	$\pm 0.01^\circ$
$\gamma$	90°	

Table 1.1: Unit cell parameters of molybdenum dioxide [6].

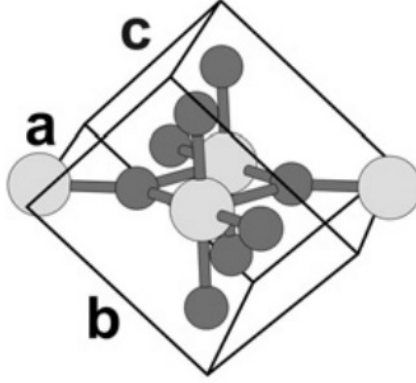


Figure 2: MoO<sub>2</sub> unit cell [7].

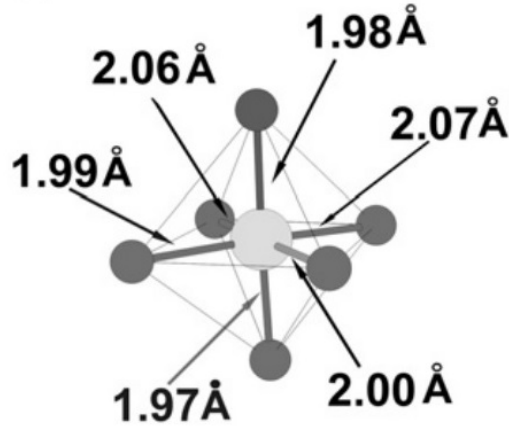


Figure 3: MoO<sub>2</sub> octahedra showing Mo-O bond lengths [7].

The distortion of the rutile structure results in long and short Mo-Mo bonds, alternating between 2.51 Å and 3.11 Å [8]. The significance, particularly of the short length, becomes more apparent when compared to the 2.725 Å length of interatomic bonds seen in metallic molybdenum. This combination of long and short bonds is responsible for the observed conductivity and results in a complex electronic structure. With molybdenum's electron configuration of [Kr]5s<sup>1</sup>4d<sup>5</sup>, after bonding with two oxygen atoms each, there are four available electrons in every Mo<sub>2</sub>O<sub>4</sub> unit. If the Mo-Mo bonds were to be single bonds, with each atom contributing an electron, there would remain two d-electrons available for

conduction. This explanation may suffice, were it not for the alternating Mo-Mo distances, one being even shorter than what is found in molybdenum metal. The short Mo-Mo bond more closely resembles a double bond than a single bond, though this would leave no electrons available for conduction, resulting in a semiconducting material. It is apparent that a simple description is not sufficient. An intermediate explanation is called for, with Mo-Mo bonds that are composed of a combination of strong sigma bonds, weaker pi bonds, and some degree of electron delocalization [9]. This results in the overlapping of the 4d electrons in short Mo-Mo bonds and is the source of molybdenum dioxide's metallic conductivity [10]. In keeping with its unusual electrical properties, MoO<sub>2</sub> has recently been reported to undergo a structural transition at 267K and an electronic transition at 220K [1].

MoO<sub>2</sub> is currently being studied as an anode material in lithium ion batteries and fuel cells [11]. In fuel cells, MoO<sub>2</sub> acts as a solid oxide anode. In current fuel cells the anode is commonly made of a nickel based mixture of a metal and a ceramic. Unlike nickel fuel cells which experience a decline in performance when used with fuels other than pure hydrogen, MoO<sub>2</sub> has demonstrated negligible reductions in performance in long term operating tests. This is due to the ability of MoO<sub>2</sub> based anodes to resist the accumulation of coke-like carbonaceous compounds that can be formed when operating a cell with hydrocarbon fuels [12].

### 1.3 Molybdenum Oxide - Mo<sub>4</sub>O<sub>11</sub>

Mo<sub>4</sub>O<sub>11</sub> is a layered crystalline ceramic and quasi-2D metallic conductor. It has an  $\eta$  phase which is stable at lower temperatures, and a high temperature  $\gamma$  phase. The  $\eta$  phase is monoclinic, while the  $\gamma$  phase has an orthorhombic structure [13]. The transition occurs at approximately 610°C and the high temperature  $\gamma$  phase can be stabilized by quenching to rapidly cool before the  $\eta$  phase transition can occur [14].

Dimension	Length/Angle
a	24.54Å
b	5.439Å
c	6.701Å
$\alpha$	90°
$\beta$	94.28°
$\gamma$	90°

Table 1.2: Unit cell parameters of  $\eta$ -Mo<sub>4</sub>O<sub>11</sub> [15].

Dimension	Length/Angle
a	24.49Å
b	5.457Å
c	6.752Å
$\alpha$	90°
$\beta$	90°
$\gamma$	90°

Table 1.3: Unit cell parameters of  $\gamma$ -Mo<sub>4</sub>O<sub>11</sub> [15].

Due to the oxidation state of the metal ions, Mo<sub>4</sub>O<sub>11</sub> 4d electrons are not readily available for conduction, thus, it acts as an insulator. The  $\eta$  phase has two phase transitions, reported to occur at 109K and 30K and attributed to charge density wave (CDW) instabilities.  $\eta$ -Mo<sub>4</sub>O<sub>11</sub> is a layered compound, composed of MoO<sub>6</sub> octahedral sites in the {100} lattice planes, with layers linked together by tetrahedral MoO<sub>4</sub> sites [16] [17].

As a layered compound Mo<sub>4</sub>O<sub>11</sub> has anisotropic physical properties. The resistivity of  $\gamma$ -Mo<sub>4</sub>O<sub>11</sub> is roughly 5 times greater along the a-axis, than the b- or c-axis with a minima occurring around 100K in all three axes on the order of 10<sup>-4</sup>Ωcm [14]. The first CDW transition occurs at a lower temperature in the  $\gamma$  phase, around 95K, and the low temperature 30K CDW instability is reported to be entirely absent [17].

## 1.4 Low Dimensional Materials

A low dimensional material is one whose properties fall between those of a single atom and a typical bulk material. Well known examples include graphene, an archetypal 2D material, and its quasi-single dimensional form, carbon nano-tubes. Although chemically identical to graphite, these lower dimensional forms display properties not seen in the common bulk phase. A telltale sign of a low dimensional or quasi-low dimensional material is anisotropic physical properties. Graphene is composed of a single layer of hexagonally arranged carbon atoms with a  $1.42\text{\AA}$  in-plane nearest neighbor distance. Graphite is composed of layers of small graphene sheets, which are weakly bonded together and have a plane separation of  $3.35\text{\AA}$ . This manifests most obviously in the case of graphite and graphene as orders of magnitude differences in tensile strength and electrical conductivity. Tensile strength is the ability of a material to resist deforming and breaking when exposed to a tension force. In the case of graphite this value can vary widely, though  $27\text{ MPa}$  [18] is a typical value, while the tensile strength of graphene has been measured by one source at  $99.34\text{ GPa}$  [19], a value more than 3000 times higher. This difference is due to the relatively weak inter-plane bonding, which causes multiple layers of graphene to display anisotropic physical properties. While graphene and graphite are an extreme example, the pair do effectively illustrate the difference that ordering of otherwise identical materials can make.

The molybdenum oxides are also anisotropic, and while they don't vary as much as graphene and graphite between samples with the same stoichiometry, they do exhibit quasi-low dimensional behaviors. One such behaviour of interest in this paper is the charge density wave, discussed in the following section.

## 1.5 Charge Density Waves

CDWs are observed in low and quasi-low dimensional materials and exist as an ordered quantum fluid, with the electrons involved producing a standing wave. Early examination of what would become known as CDWs began with Peierls transitions, which are a form of lattice distortion in 1-D crystals. This transition takes the form of dimerization and is due to the instability of equidistant electrons in 1-D chains [20]. The distortion brings the crystal lattice into a higher energy state, which is then overcompensated for by the corresponding drop in electronic energy [21], resulting in a lower energy state. This was initially postulated as a potential mechanism of high temperature superconductivity due to the similarity to Cooper pairing, specifically, electron-electron attraction mediated by positively charged ions and the formation of bosonic quasi-particles. Early experiments examining Peierls transitions focused on long chain organic molecules with partially filled conduction bands. However, instead of undergoing a superconducting transition, the materials became insulators when cooled below their transition temperature [20]. Instead of uncovering high temperature superconductivity, researchers had discovered CDWs.

## 1.6 Chemical Vapour Transport

Chemical Vapour Transport (CVT) is a gas phase reaction in which a nonvolatile precursor is volatilized by a transport agent, to be transported by diffusion to a location in which deposition is energetically favourable. This chemical reaction can be seen at work in halogen lamps. Tungsten sublimating off the filament is deposited on the glass bulb, then revolatilized by iodine or bromine. This tungsten halide will remain gaseous until contacting the filament where the high temperature causes the compound to decompose, depositing metallic tungsten on the filament, releasing the halogen, and completing the cycle. Beyond this every day example, CVT is used experimentally and industrially in the



production of certain high purity substances, such as zirconium in the iodide process [22], and in single crystal growths.

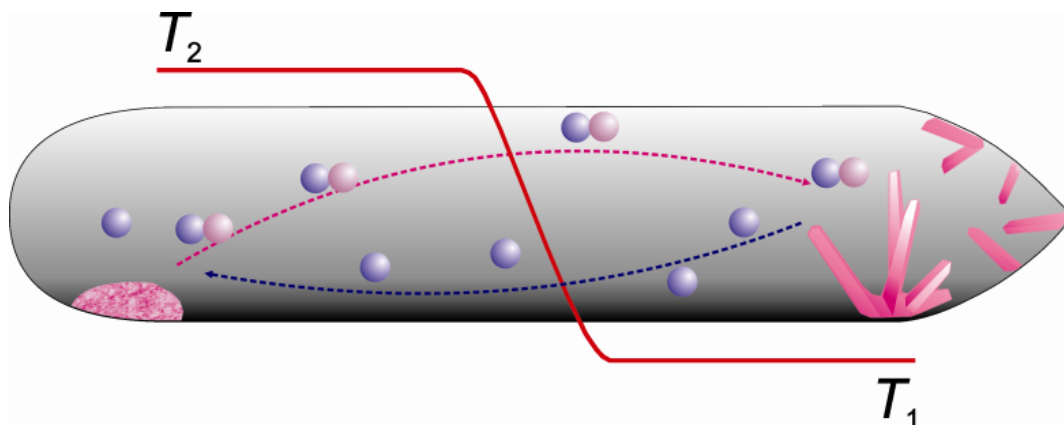


Figure 4: Crystal growth by chemical vapour transport, with precursor formed into a volatile intermediate compound by a transport ion and transported along a temperature gradient [23].

For a growth to be successful certain conditions must be met. First, appropriate precursors must be present, typically a combination mixed in a stoichiometric match to the desired product. A transport ion, or a material which will decompose and provide a transport ion must also be chosen, unless sufficient vapour pressure of the reagents can be achieved through heating alone. This transport ion is necessary as it will temporarily combine with your source materials and form a volatile intermediate. Now temperatures must be selected, which, if using a transport agent, will be dictated by the Gibbs energy of formation of the volatile intermediate. The energy of formation should fall within a range of  $-100\text{kJ/mol}$  and  $100\text{kJ/mol}$ , having a negative value on the source side in order for the volatile intermediate to form. Once the intermediate has moved up or down the temperature gradient, the energy of formation in the new temperature of the growth zone should be positive, so that the intermediate can decompose [23].

## 1.7 Four Probe Resistivity

The linear four probe method was chosen over the van der Pauw type four probe sensing due to the anisotropy of the samples and their less than ideal shape. The van der Pauw method would have provided a measured resistance value that was a mix of the two axis in the plane of the chosen sample while the four probe method measures along the axis of the contacts. Additionally the long rectangular shape and small size of the samples would have resulted in an undesirable ratio of contact size to separation. Samples were typically on the order of 1mm wide, 3mm long, and 0.5mm thick.

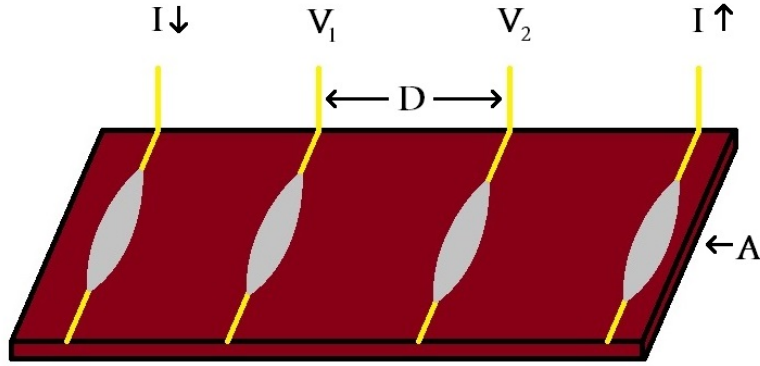


Figure 5: Four probe method setup showing the arrangement of gold wire contacts attached by colloidal silver paste.

$$\rho = \frac{V_1 - V_2}{I} \cdot \frac{A}{D} \quad (1)$$

In the four probe method resistivity is found using equation 1 where I is the current through the sample,  $V_1$  and  $V_2$  are the voltages at two different points separated by a distance D, and A is the cross-sectional area perpendicular to the current.



Figure 6: Van der Pauw method showing the arrangement of gold wire contacts attached by colloidal silver paste. This image shows the contact orientation for  $R_1$ , for  $R_2$  the contact positions would be rotated  $90^\circ$  clockwise.

Using the Van der Pauw method, the average sheet resistance of the sample is solved for using equation 2

$$e^{-\pi R_1/R} + e^{-\pi R_2/R} = 1 \quad (2)$$

where  $R_1$  and  $R_2$  are calculated using equations 3 and 4

$$R_1 = \frac{V_4 - V_3}{I_{12}} \quad (3)$$

$$R_2 = \frac{V_3 - V_2}{I_{41}} \quad (4)$$

This method also requires a large distance between contacts relative to the size of the contacts to provide accurate measurements. Additionally, this method works best when the thickness of the sample is much less than the length or width. Thus the small size, non-ideal shape, and in particular the anisotropy of the sample preclude the use of the Van der Pauw method for the materials being studied.

## 1.8 Objectives

### 1.8.1 Sample Preparation

The first objective was the successful growth of  $\text{MoO}_2$  single crystals using either  $\text{I}_2$  or  $\text{TeCl}_4$ . Completion of this goal was instrumental in progressing in all other areas of this research project. Initial plan was to use chemical vapour transport utilizing  $\text{I}_2$  with growth conditions based on those described by Oppermann [24] which reported good results producing single crystal  $\text{MoO}_2$ . Later growths will use  $\text{TeCl}_4$ , which decomposes to provide chlorine as a halogen source.

### 1.8.2 Resistivity

The primary focus of this research is the examination of reported electronic and structural transitions in  $\text{MoO}_2$  around 220K and 267K respectively [1]. In examining the resistive properties of  $\text{MoO}_2$ , temperatures between 3-400K will be investigated. This will include zero field cooling (ZFC) and various field cooling (FC) measurements for both AC and DC resistivity measurements. Measurements on  $\text{Mo}_4\text{O}_{11}$ , which grew alongside the  $\text{MoO}_2$  samples will also be performed and examined. In the case of  $\text{Mo}_4\text{O}_{11}$  the focus will be on the reported 109K transition [16] and the potential for this transition to involve CDWs.

### 1.8.3 Heat Capacity

Specific heat measurements are to be performed in conjunction with resistivity measurements. The primary purpose of these measurements is further examination of possible phase transitions, particularly around the 220K and 267K transitions along with any other points of interest as they are identified. These heat capacity measurements are meant to make it possible to determine the order of the transition and reduce the possibility that any features are overlooked.

#### 1.8.4 Temperature dependent X-Ray Diffraction

At the outset of this project the Rigaku X-Ray Diffractometer available had no means of controlling sample temperature, as a result, measurements were performed at the 30-35°C of the diffractometer interior. Given the 267K transition reported in MoO<sub>2</sub> [1] constructing a cooler capable of cooling a sample below -6°C seemed entirely feasible. A previous student had attempted to construct such a temperature controller and the components they had acquired were used as a starting point. This included an assortment of peltier heater/coolers, an ATEC 203 controller, and power supplies and a pulse width modulator (PWM). Additionally a housing unit for all of these components had been 3D printed with the help of the Brock Maker Space. The intent of this portion of the project was to make this controller operational and optimize it to the point that it could cool a sample below the reported MoO<sub>2</sub> structural transition. Room temperature measurements are also necessary to confirm the identity of samples through powder diffraction and to aid in orienting single crystal samples.

## 2 Methods

### 2.1 Crystal Growth

All samples were grown using chemical vapour transport (CVT) Which produced single crystals of varying quality, highly dependent on the conditions of the growth. An illustration can be seen in figure 4 where T2 is the source zone and T1 is the growth zone. Growths were performed in fused quartz ampules with approximately 1cm inner diameter and 25cm length. All ampules were first attached to the turbo pump and evacuated while empty for at least one day and heated to remove any water trapped in the fused quartz ampule, the disconnected and filled with materials using a long necked funnel. When iodine was used as the transport ion, the portion of the ampule containing the solid iodine was submerged in liquid nitrogen for the duration of the second evacuation and the seal of the ampule, to minimize sublimation. When tellurium chloride was used instead of iodine the ampule was evacuated, mechanically closed with a glass stopcock, and transferred into a dry box where it was opened and the materials were added. The ampule was then reclosed with the stopcock, removed from the dry box to be returned to the pump, evacuated, and sealed off with a torch. Growths were then performed in a three zone tube furnace, which provided linear temperature gradients and very accurate control of the temperatures at the ampules endpoints.

Since the  $\text{MoO}_x$  halogen reaction is endothermic the transport direction is always from the hot zone to the cold zone [23].

The first successful growth was performed using a  $900^\circ\text{C}$  source zone and at  $700^\circ\text{C}$  growth zone. A 2g source charge of  $\text{MoO}_3$  99.999% and  $\text{MoO}$  99.95% mixed in a three to one by weight ratio was thoroughly ground together and added to the ampule using a long necked funnel. Next a 0.9g piece of solid iodine was placed in the ampule which was then sealed off as described above.

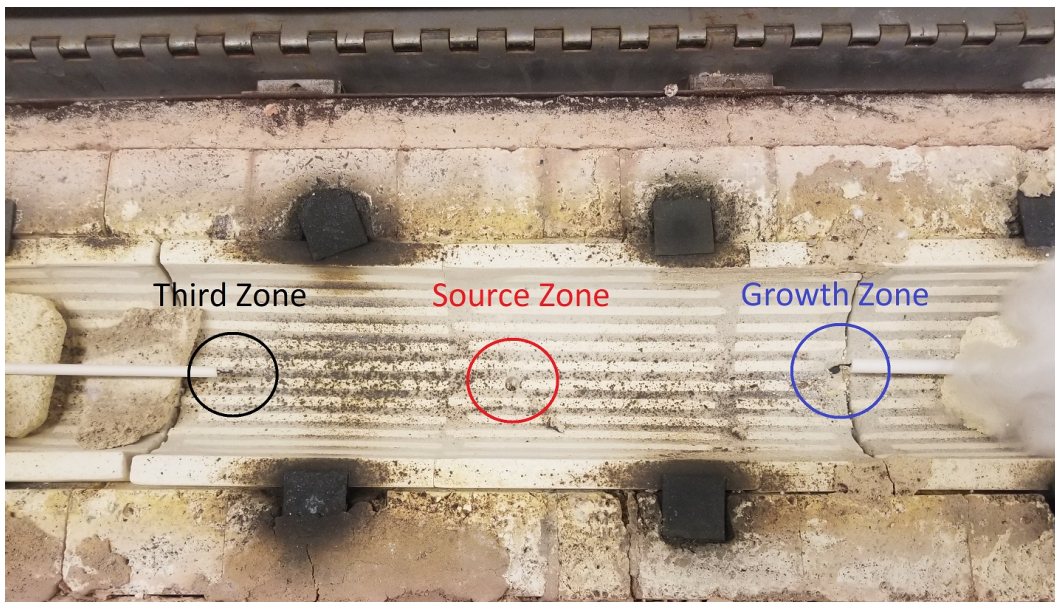


Figure 7: The three zones of the furnace used. The third zone was set to a suitable temperate to assure that the source zone's temperature would remain steady.

Duration	Zone Three	Source Zone	Growth Zone
	30°C	30°C	30°C
5 hours			
	850°C	900°C	700°C
144 hours			
	850°C	900°C	700°C
5 hours			
	30°C	30°C	30°C

Table 2.1: Temperatures for each of the three zones and soaking and ramping times for each set temperature.

The result of this growth was a large number of small crystals coating the last four centimeters of the walls of the ampule and complete consumption of the reactants. Iodine can be seen, condensed along the length of the ampule, which sublimated away after the crystals were extracted. These crystals were brown/bronze in colour with the largest ones having single sides as long as 2mm. Based on the results of later growths it appears that

excessive pressure caused by the relatively large  $I_2$  charge was the reason why so many small crystals were produced. Later growths with similar conditions but 0.1-0.2g of iodine produced fewer, larger crystals, without consuming all of the source side reactants.

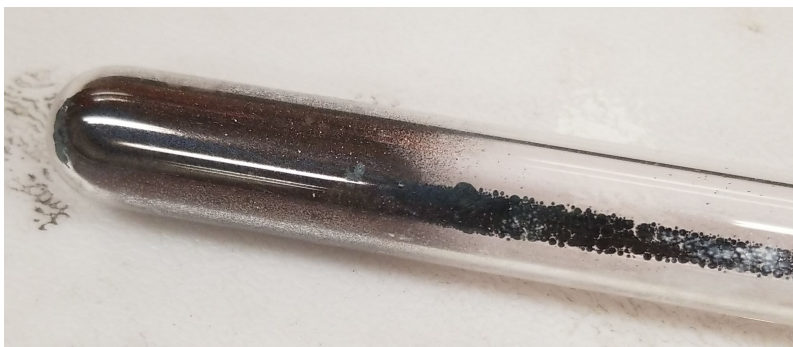


Figure 8: Ampule after first CVT growth, crystals can be seen at the end of the growth side and a line of condensed iodine can be seen along the length of the ampule.



Table 2.2:  $MoO_2$  crystals from the second  $I_2$  growth.

Different temperature profiles for the iodine transport growths were also tried but with limited success. Increasing the source side temperatures from  $900^{\circ}C$  had little impact on transport success, though sometimes resulted in the furnace struggling to hold its set temperature in the cold zone. Decreasing the temperature on the source side reduced the total crystal formation and in one instance a polycrystalline layer or lump formed on the exposed area of the reactants. This also may have been due to the 24 hour back transport



reaction performed during this growth. Back transport steps were not implemented in later growths as no benefits were observed. When growth side temperatures were reduced the number of crystals formed increased, but the total size decreased significantly. Crystals were also observed to form closer to the source side of the ampule. Increasing the temperature of the growth side drastically reduced the total growth yield, although, did not significantly impact the size of crystals. At higher growth-side temperatures total yield appeared to become dependent on the amount of iodine available for transport.

When iodine was replaced with tellurium chloride the results of the growth changed significantly. In one growth a 2g charge was placed in the ampule along with 0.1g of  $\text{TeCl}_4$ . This growth was successful, using the  $900^\circ\text{C}$  and  $700^\circ\text{C}$  furnace settings and an 11 day transport time. The results of this growth diverged significantly from the iodine transport reactions. Upon removal from the furnace the ampule was visibly frosted from the inside, once opened this frosting was observed to be light pocketing and roughening of the inside of the ampule. The source charge had been entirely consumed and crystals had grown much larger than in any other growth. The crystals had their sharp edges dulled and rounded, and were coated in a thick, dark, blue/green liquid which dissolved in acetone and stained the inside of the beaker in which it was dissolved. All tools used in extraction and handling of the crystals, even though cleaned after use, rusted where they had come into contact with the crystals. Based on the appearance, available elements, and corrosive nature of the material it appears to have been molybdenum(V) chloride. Once cleaned in acetone the crystals took on the same colour as previous  $\text{MoO}_2$  crystals grown using  $\text{I}_2$  transport, though some twinning of the crystals was apparent. One large crystal of  $\sim 3\text{x}3\text{x}6\text{mm}^3$  was prepared by grinding and polishing for resistivity measurements. The results were erratic and so the crystal, seen in figure 9 was cleaved. The inside of the crystal was composed of distinct sections, both the familiar bronze of  $\text{MoO}_2$  and a purple colour initially believed to be  $\text{Mo}_4\text{O}_{11}$ . Later X-ray diffraction of these crystals showed them to be made up primarily

of  $\text{MoO}_2$  and  $\text{Mo}_9\text{O}_{26}$ , a small amount of  $\text{MoO}_3$ , with no measurable quantity of  $\text{Mo}_4\text{O}_{11}$  present.



Figure 9: Two halves of a cleaved  $\text{TeCl}_4$ -grown crystal showing irregular surface and mixing of colours and textures.

## 2.2 X-Ray Diffraction

All X-ray diffraction (XRD) measurements were performed on a Rigaku SmartLab X-ray diffractometer. For these measurements the X-ray tube was powered with 40kV at 44mA. Scans were typically performed over a  $10\text{-}90^\circ$  range, although in some instances  $15^\circ$  was used as a starting point when repeating measurements when no peaks were present at lower angles.

### 2.2.1 Powder Diffraction

Powder diffraction was done to confirm the identity of the crystals in each growth and identify any additional growth products or contaminants. Samples from each growth were

selected based on size and cleanliness. Samples too small to readily attach contacts or with irregular shapes that would be difficult to polish into a rectangular shape opposite a single clean crystal face were set aside. From these crystals rejected for resistivity measurements, glass from the growth within the ampule was carefully removed while examining each crystal under a microscope. These now cleaned small and damaged crystals were then ground under acetone with a mortar and pestle. After drying the powder was placed on a quartz well slide in the diffractometer and Bragg-Brentano general focusing measurements were then performed. Scanning times varied depending on machine availability and clarity of peaks in initial measurements.

### **2.2.2 Single Crystal Diffraction**

In order to determine the orientation of the samples used for four probe resistivity measurements, single crystal x-ray diffraction measurements were performed. All measurements on single crystals used the Rigaku preset general measurement setting (high resolution PB-Ge(220)x2). Samples were first cleaned then placed on a slide in the diffractometer. Sample alignment was performed, followed by short (roughly five minute) general measurement scans to locate the sample on the platform. The sample was shifted and the scan was repeated until a peak could be seen in the intensity result. This peak indicated that the sample was positioned acceptably in the path of the beam, resulting in an adequate reflection. A higher resolution scan was then performed and peaks in this result were compared to the peaks in analyzed powder diffraction results.

### **2.2.3 Temperature Control**

On taking over the project to build a temperature controlled sample platform for the Rigaku x-ray diffractometer, the components available were not compatible. The power supply was providing enough current to burn out the peltier before the thermistor, controller, and pulse

width modulator (PWM) could reduce the current being supplied. Larger peltier coolers were ordered and once the 14W unit was replaced with a 40W unit, rated for 15V, the system was capable of reaching stable temperatures.



Figure 10: 2x2cm<sup>2</sup> 14W and 3x3cm<sup>2</sup> 40W Thermoelectric coolers

With the original air cooled aluminum heat sink, increasing temperatures as high as 75°C was manageable, but attempting to bring the sample platform more than a few degrees below room temperature would result in thermal run away. The finned aluminum heat sink was not capable of dissipating enough heat and a more effective design was needed.



Figure 11: Finned aluminum heat sink seated inside 3D printed housing, cooling fan absent.

A solid heat sink with a hole bored through for a half inch copper pipe was made. With this copper pipe extending out and into a container of liquid nitrogen the sample holder could be cooled down to  $-50^{\circ}\text{C}$  in a  $25^{\circ}\text{C}$  room. Even with the low temperature, high mass heat sink, the peltier was still capable of bringing the sample up to room temperature, a  $+70^{\circ}\text{C}$   $\Delta T$ . While this allows for stable temperatures to be held for as long as the nitrogen reservoir remains, as temperatures drop condensation becomes a serious issue. While condensation on the sample platform occurs, this is mitigated by a cover with two kapton windows.

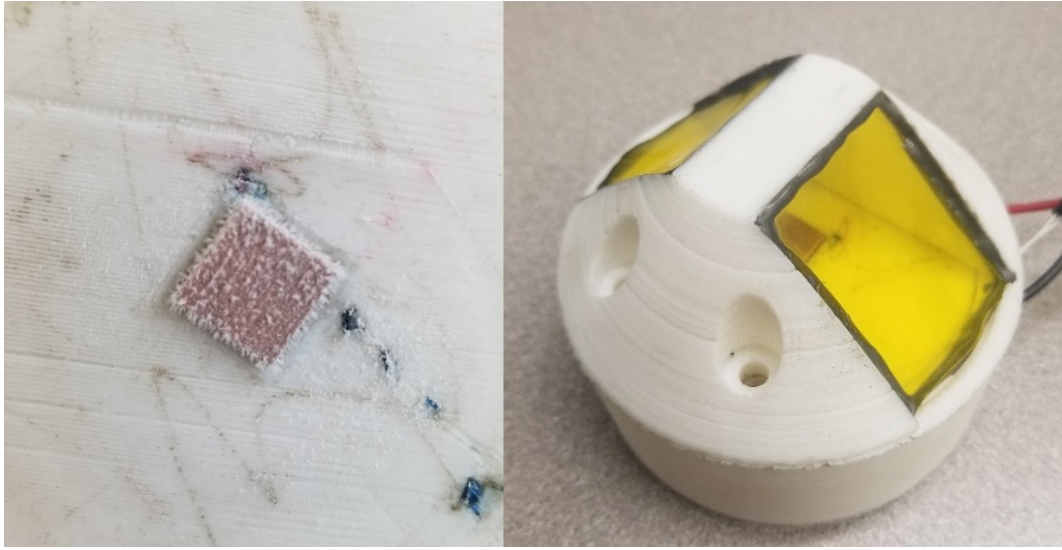


Figure 12: Uncovered sample platform icing over and assembly with sample cover in place.

Unfortunately condensation on the rest of the temperature controller presented a similar problem on a larger scale, with the entire heat sink icing over. It was hoped that the cover seen above, with two kapton windows, would sufficiently limit airflow to avoid this problem. Unfortunately, without further measures to avoid condensation and icing, low temperature measurements are not possible. Possible solutions included evacuating the sample chamber and flooding the sample chamber with dry nitrogen gas, though time and machine availability limited the ability to implement potential solutions. High temperature measurements were still possible, though accuracy was limited by the rated range of the thermistor. The maximum operating temperature of the  $2252\Omega$  thermistor was  $150^{\circ}\text{C}$  though it was only rated as accurate within  $\pm 0.1^{\circ}\text{C}$  up to  $70^{\circ}\text{C}$ .



Figure 13: Heat sink encased in ice during testing.

## 2.3 Resistivity Measurements

A Quantum Design Physical Properties Measurement System (QD PPMS) was used for the majority of the resistivity measurements. Measurements were performed between 3.5-400K, both with samples cooled within an applied magnetic field, called field cooled (FC) and with no applied field, called zero field cooled (ZFC). The frequency of the current ranged from 1-1000Hz, the upper and lower limit of the PPMS. Measurements were performed under vacuum, which is essential to prevent the condensation and freezing of atmospheric gasses on the sample.

### 2.3.1 Direct Current Resistivity Measurements

A small number of additional measurements were performed in a DC cryostat using a CRYO-TORR 8 high vacuum pump and CTI CRYOGENICS 8001 controller, a 8300 helium compressor and a DRC-91C temperature controller. This apparatus was used to investigate an unexpected peak appearing in the  $\text{MoO}_2$  resistivity results obtained with the PPMS. Compared to the PPMS, the cryostat had relatively limited temperature con-



trol. A manually operated  $50\Omega$  resistance heater was constructed of niobium wire covered with quartz fiber insulation and then wrapped around the the copper sample platform. This allowed temperatures to be reliably elevated to 400K. The cryostat itself was capable of cooling down to 15K when given sufficient time, although below 20K the temperature was unstable.



Figure 14: Sample mounting puck of the DC cryostat.

## 2.4 Heat Capacity

The QD PPMS was also used to perform heat capacity measurements from 400K down to 5K. Measurements were performed in two stages, from 400K to 200K and then from 205K down to 5K. This was done because there was no vacuum grease, necessary to maintain thermal contact between the sample and platform, available which could reliably perform



across the entire temperature range. The sample holder used had already been calibrated and so re-calibration was not performed, although prior to each experiment the values of the sample holder and the PPMS thermostats were checked and found to be in agreement. An addenda measurement was then made, with apiezon N or H grease, depending on the temperature range of the upcoming measurement, carefully applied to the platform, sample absent. After this addenda measurement, the sample was weighed then placed onto the sample platform, with care taken to avoid removing any grease or introducing anything other than the sample.



Figure 15: Heat capacity puck, samples are placed on the central platform, with a small amount of grease to prevent movement and ensure good thermal contact.

The system works via carefully controlled heating of the platform and, through the thermally conducting grease, the sample, followed by a period of cooling. Since measurements are performed with the system evacuated of gas, heat is dissipated from the sample almost exclusively by conduction through the wires which suspend the platform. The thermometer below the platform measures the temperature as the sample and platform are heated by a resistor and then allowed to cool. With the heat being put into the system

by the resistor being known and the change in temperature, along with the heat lost to conduction being known, the heat capacity of a sample can be accurately measured as a function of temperature [25].

## 3 Results

### 3.1 X-Ray Diffraction

#### 3.1.1 Powder Diffraction - Identification

X-ray powder diffraction was performed on crystals from the iodine growths which had been visually identified as  $\text{MoO}_2$ . The x-ray diffraction shown in figure 18 confirmed their composition as pure  $\text{MoO}_2$  with the following lattice parameters.

Dimension	Length/Angle
a	5.6126(4)Å
b	4.87257(9)Å
c	5.6409(4)Å
$\alpha$	90.000000°
$\beta$	120.881(3)°
$\gamma$	90.000000°

Table 3.1: Unit cell parameters of  $\text{I}_2$  Grown  $\text{MoO}_2$ .

In addition to the  $\text{MoO}_2$  crystals in the iodine growths, visually distinct purple crystals were discovered. Powder diffraction tests on these purple samples revealed them to be  $\text{Mo}_4\text{O}_{11}$ . It was necessary to include some  $\text{Mo}_4\text{O}_{11}$  with quantities of  $\text{MoO}_2$  attached, in order obtain a sufficient quantity of powder. The mixed powder sample was measured by the diffractometer was 29.1(11)%  $\text{Mo}_4\text{O}_{11}$  and 70.9(12)%  $\text{MoO}_2$ . The  $\text{Mo}_4\text{O}_{11}$  were orthorhombic with dimensions as follows.

Dimension	Length/Angle
a	24.4640(4)Å
b	5.45259(10)Å
c	6.74661(13)Å
$\alpha$	90.000000°
$\beta$	90.000000°
$\gamma$	90.000000°

Table 3.2: Unit cell parameters of I<sub>2</sub> Grown Mo<sub>4</sub>O<sub>11</sub>.

With a  $\beta$  angle of 90° the crystals are  $\gamma$ -Mo<sub>4</sub>O<sub>11</sub>. This is unexpected as  $\eta$ -Mo<sub>4</sub>O<sub>11</sub> is the low temperature stable phase, while  $\gamma$ -Mo<sub>4</sub>O<sub>11</sub> is formed by heating above 600°C and quenching. The samples produced here however were cooled from 700°C down to room temperature over a period of five hours.

Analysis performed on the TeCl<sub>4</sub> samples identified 79.8(12)% MoO<sub>2</sub>, 4.6(5)% MoO<sub>3</sub> (identified as synthetic molybdate), and two phases of Mo<sub>9</sub>O<sub>26</sub> making up 10.5(10)% and 5.1(8)%.

Dimension	Length/Angle
a	16.68(3)Å
b	4.0224(16)Å
c	14.404(13)Å
$\alpha$	90.000000°
$\beta$	95.79(7)°
$\gamma$	90.000000°

Table 3.3: Unit cell parameters of the first phase TeCl<sub>4</sub> grown Mo<sub>9</sub>O<sub>26</sub>.

Dimension	Length/Angle
a	29.914(13)Å
b	7.9863(8)Å
c	16.642(16)Å
$\alpha$	90.000000°
$\beta$	94.85(6)°
$\gamma$	90.000000°

Table 3.4: Unit cell parameters of the second phase of  $\text{TeCl}_4$  grown  $\text{Mo}_9\text{O}_{26}$ .

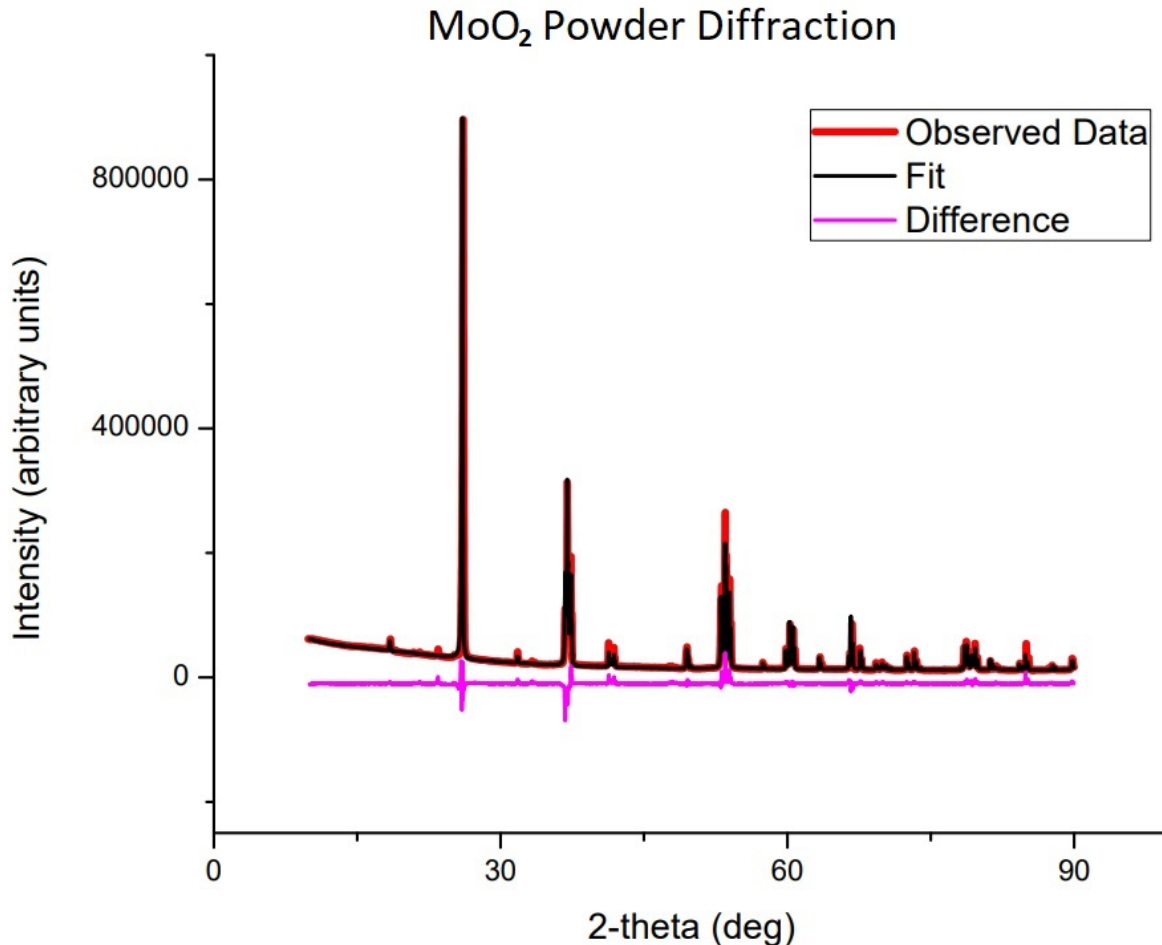


Figure 16: Powder diffraction peaks of MoO<sub>2</sub> grown using I<sub>2</sub> transport agent.

Powder diffraction results for MoO<sub>2</sub> with the recorded intensity in red and the Rietveld fit in black, and the difference between the two in magenta. The peak list can be seen in table A.1 in appendix A. MoO<sub>2</sub> was found to be a match by the PDXL software used with a figure of merit of 0.304. Rietveld analysis with the same PDXL program using phase details from the Inorganic Crystal Structure Database (ICSD), database card number 152316, gave an S value of 10.9532. This is a surprisingly high S value, given how small the difference between the data and fit appears to be. This can be partially accounted for by the fact that the analysis was performed over the full 10°-90° range of the scan which included multiple

clustered peaks.

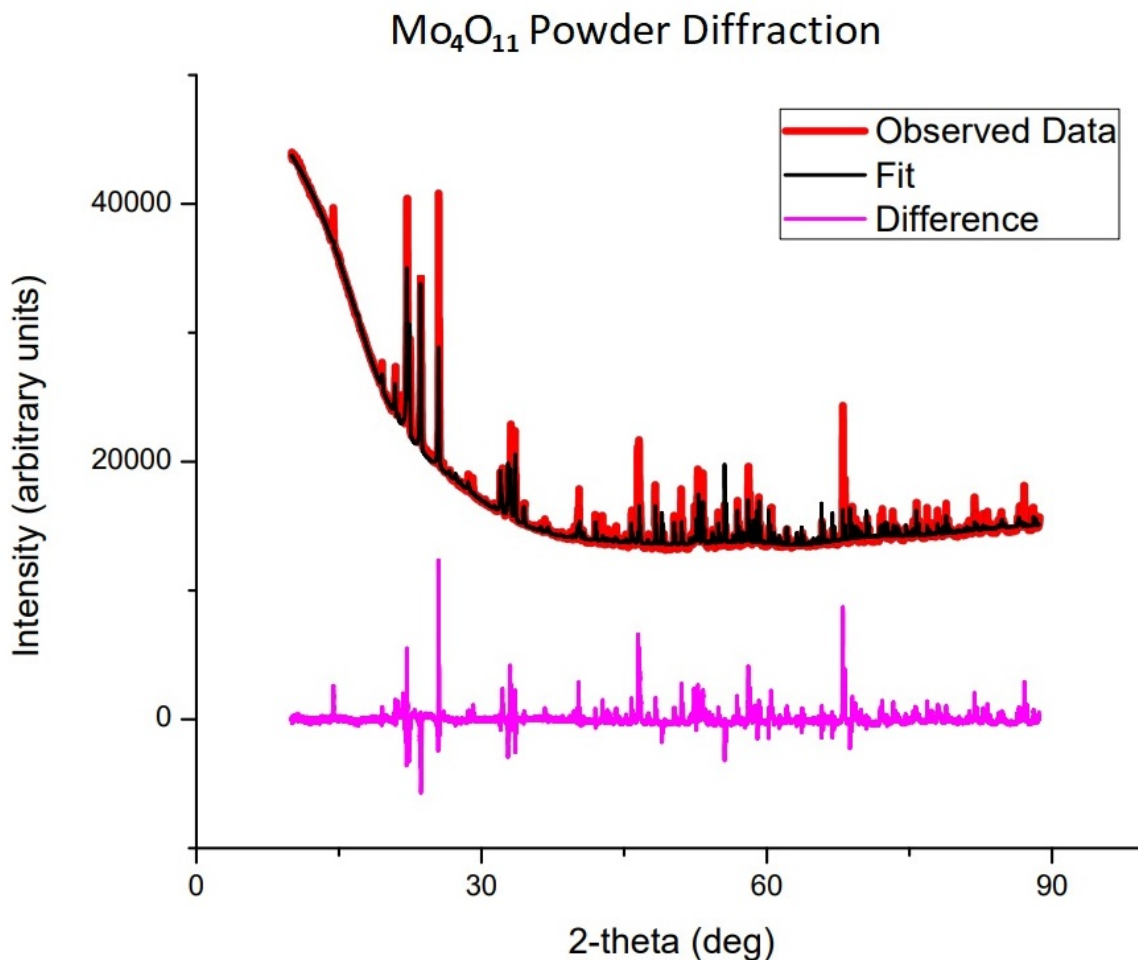


Figure 17: Powder diffraction peaks of Mo<sub>4</sub>O<sub>11</sub> grown using I<sub>2</sub> transport agent.

Powder diffraction results for Mo<sub>4</sub>O<sub>11</sub> with the recorded intensity in red and the Rietveld fit in black, and the difference between the two in magenta. The peak list can be seen in table A.2 in appendix A. The Mo<sub>4</sub>O<sub>11</sub> matched with a figure of merit of 1.056, to database card number 201573 of the ICSD. The Rietveld analysis had an S value of 3.9569, which is larger than would be ideal, but makes sense given the large background, multitude of peaks, and the fact that analysis was performed over the full scan range.

### 3.1.2 Single Crystal Diffraction - Orientation

Identifying the planes of the faces of single crystals was necessary due to the anisotropic nature of the materials being studied.

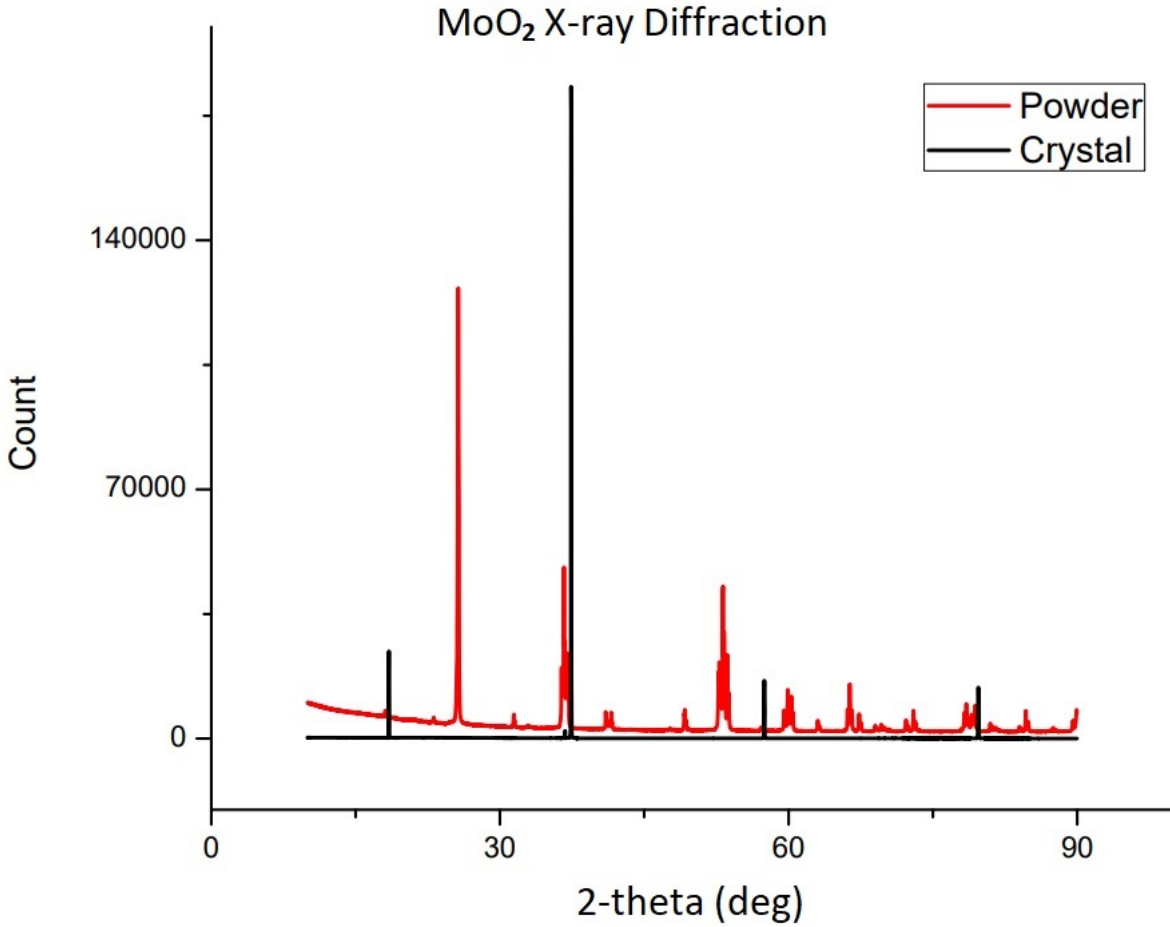


Figure 18: Diffraction peaks of powder and single crystal samples of MoO<sub>2</sub>.

The single crystal peaks correspond to the (100) plane at 14.4°, (200) at 37.3°, (300) at 57.4°, and the (400) plane at 79.6°. The single crystal diffraction peaks were consistently shifted by approximately 0.07° to the right of the powder diffraction peaks. This may be explained by the grinding of the bottom of the sample not being perfectly parallel to the opposite crystal face, or a slight change in the diffraction angle due to the thickness of the



sample. An additional, relatively short peak can also be seen at  $36.7^\circ$  which most closely matches the  $(-2,0,2)$  plane.

With the top face being parallel to the  $(100)$  plane, the long axis, along which resistivity measurements were made must be along the b-axis, c-axis, or at an angle in between. Using the flux growth methods, authors have reported a tendency for  $\text{MoO}_2$  to grow longest along the c-axis, though this was reported with crystals having faces most often parallel to the  $(110)$  plane [26].

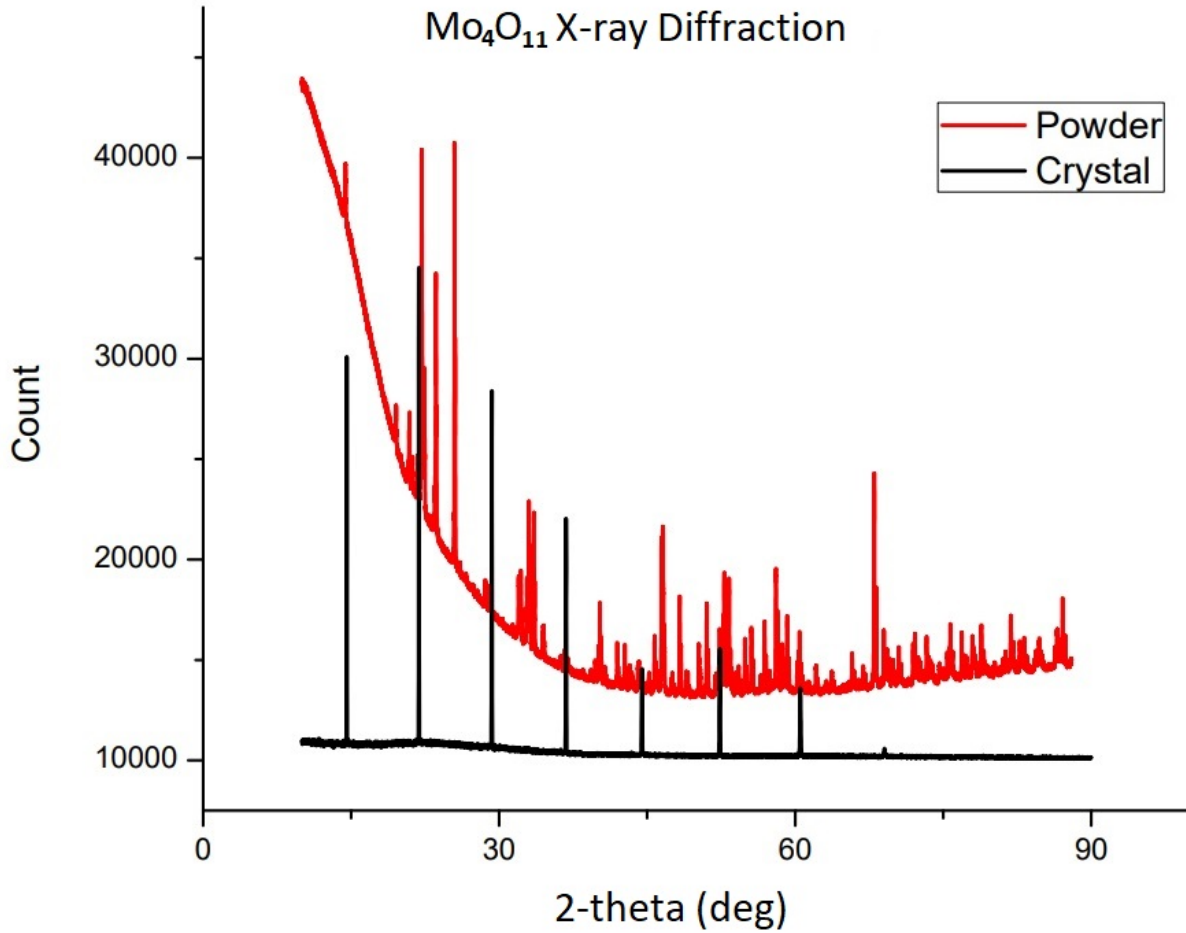


Figure 19: Diffraction peaks of powder and single crystal samples of  $\text{Mo}_4\text{O}_{11}$ .

The  $\text{Mo}_4\text{O}_{11}$  x-ray diffraction peaks shown in figure 19 correspond to the  $(400)$  plane

at  $14.4^\circ$ , (600) at  $21.7^\circ$ , and (800) at  $29.1^\circ$ , with the pattern continuing. The peaks of the single crystal sample were consistently shifted to the right of the powder diffraction samples by roughly  $0.13^\circ$ , indicating that the crystal face was not perfectly parallel to the sample plate. Thus, resistivity measurements performed on this crystal were performed in the b-c plane of the crystal, and were along the b-axis, c-axis, or some combination of the two.  $\text{Mo}_4\text{O}_{11}$  is a layered compound with layers running parallel to the b-c plane and stacking on the a-axis, which means all resistivity measurements were taken along the  $\text{MoO}_6$  octahedra and  $\text{MoO}_4$  tetrahedra, rather than perpendicular. Long plate-like growth with samples having a large (100) crystal face is typical for  $\text{Mo}_4\text{O}_{11}$  [14],[27].

## 3.2 MoO<sub>2</sub>

### 3.2.1 Iodine Transport Growth

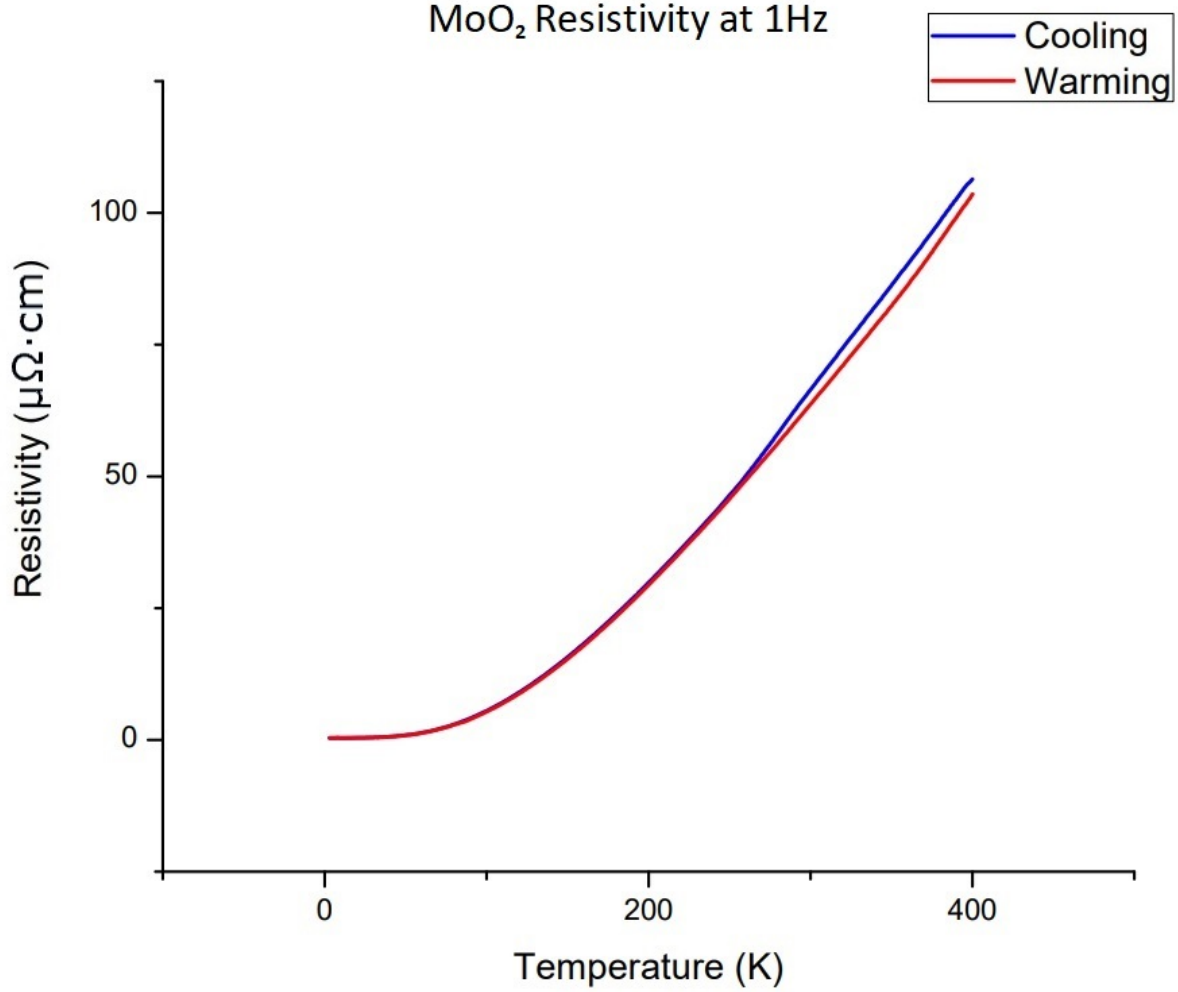


Figure 20: Resistivity of MoO<sub>2</sub> measured along the a-axis using a QDPPMS, at 1Hz AC. Sample is from the second I<sub>2</sub> CVT growth, showing hysteresis starting around 260K-270K.

The separation of the cooling and warming curves can be seen in figure 20 occurring around the 267K temperature reported in other works indicating there may in fact be a structural first-order phase transition. The magnitude of the separation however is much smaller than

reported [1].

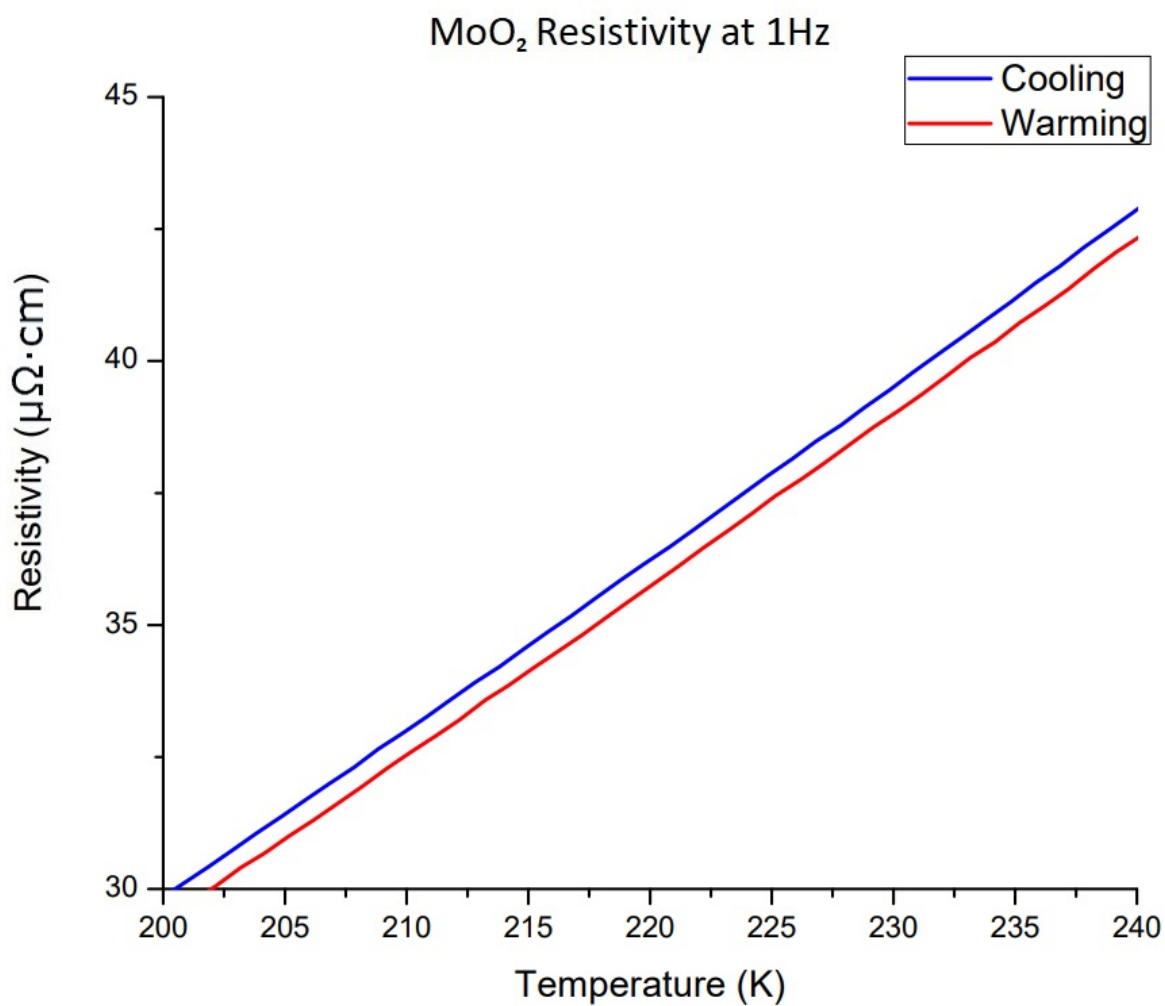


Figure 21: Resistivity of MoO<sub>2</sub> examined around 220K where an electronic-type transition has been reported to occur [1].

At 220K there is no indication in the resistivity that a transition is occurring.

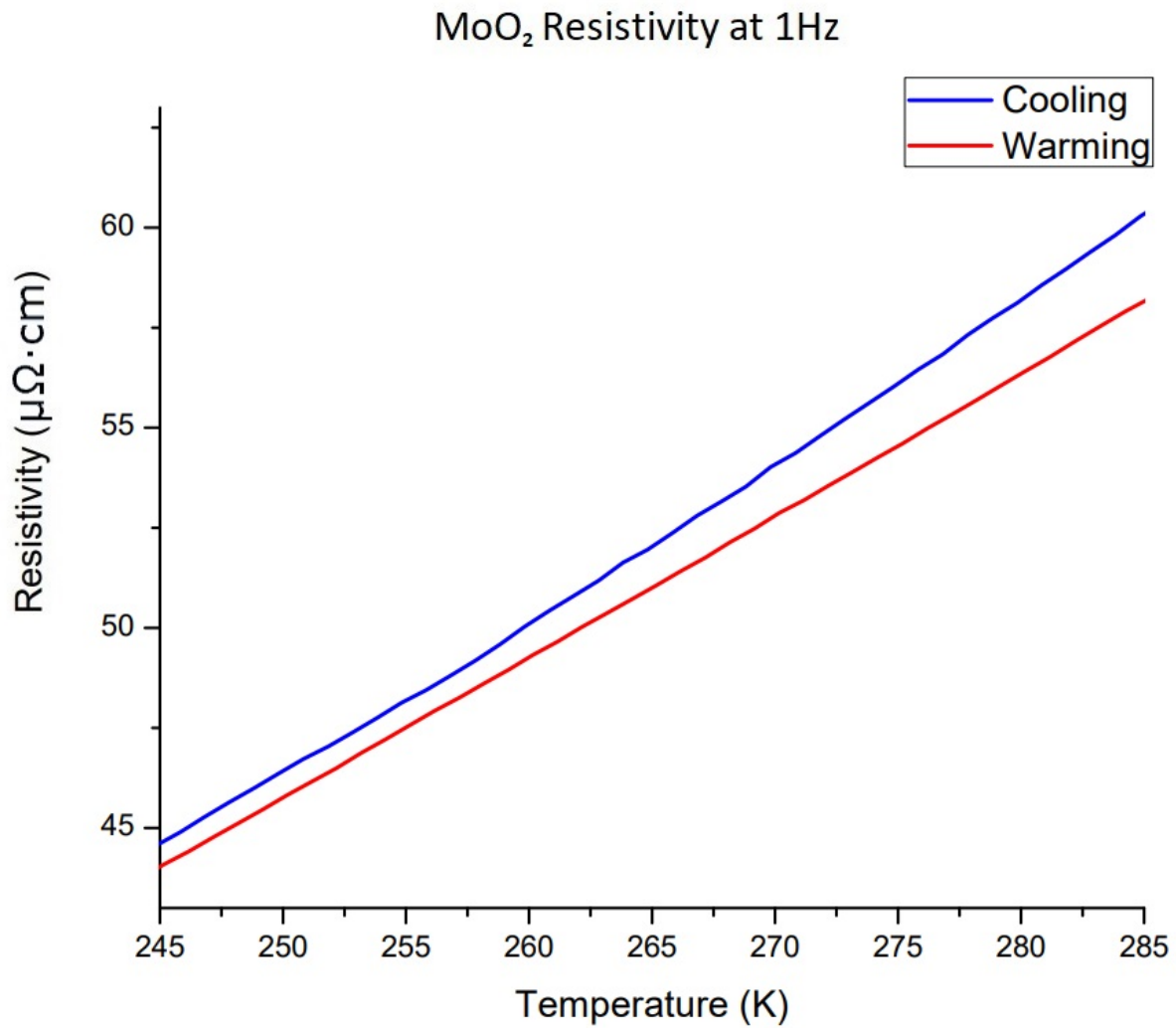


Figure 22: Resistivity of MoO<sub>2</sub> examined around 267K where a phase transition has been reported to occur [1].

On close inspection hysteresis in the resistivity of the sample can be seen, with divergence beginning between the warming and cooling curves as the sample warms above 260K.

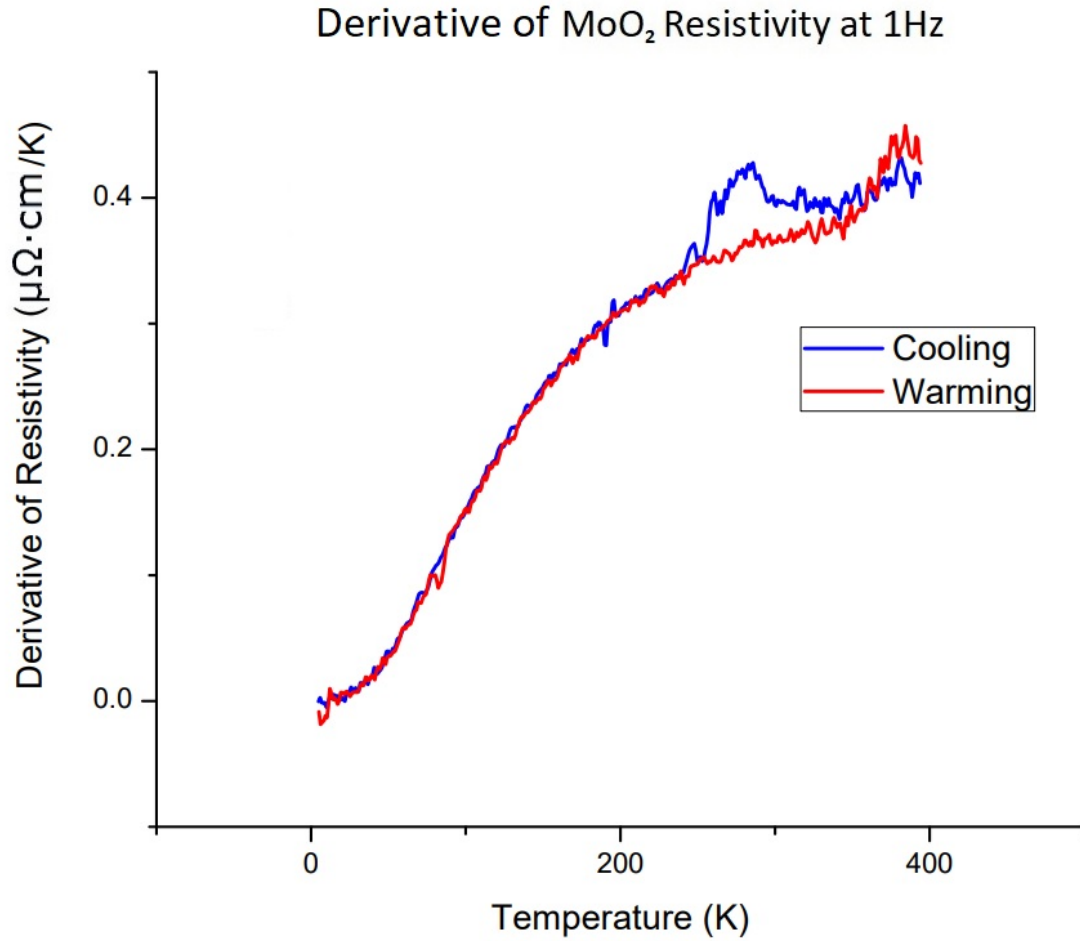


Figure 23: Derivative of the cooling and warming.

Examining the derivative, the location and temperature separation of the transition can be seen more clearly. The peaks are separated by almost 100K and so the transition can only be said to occur around 267K on cooling, on warming it doesn't occur until 360K. As in the resistivity versus temperature graphs, no evidence of a 220K transition is apparent.

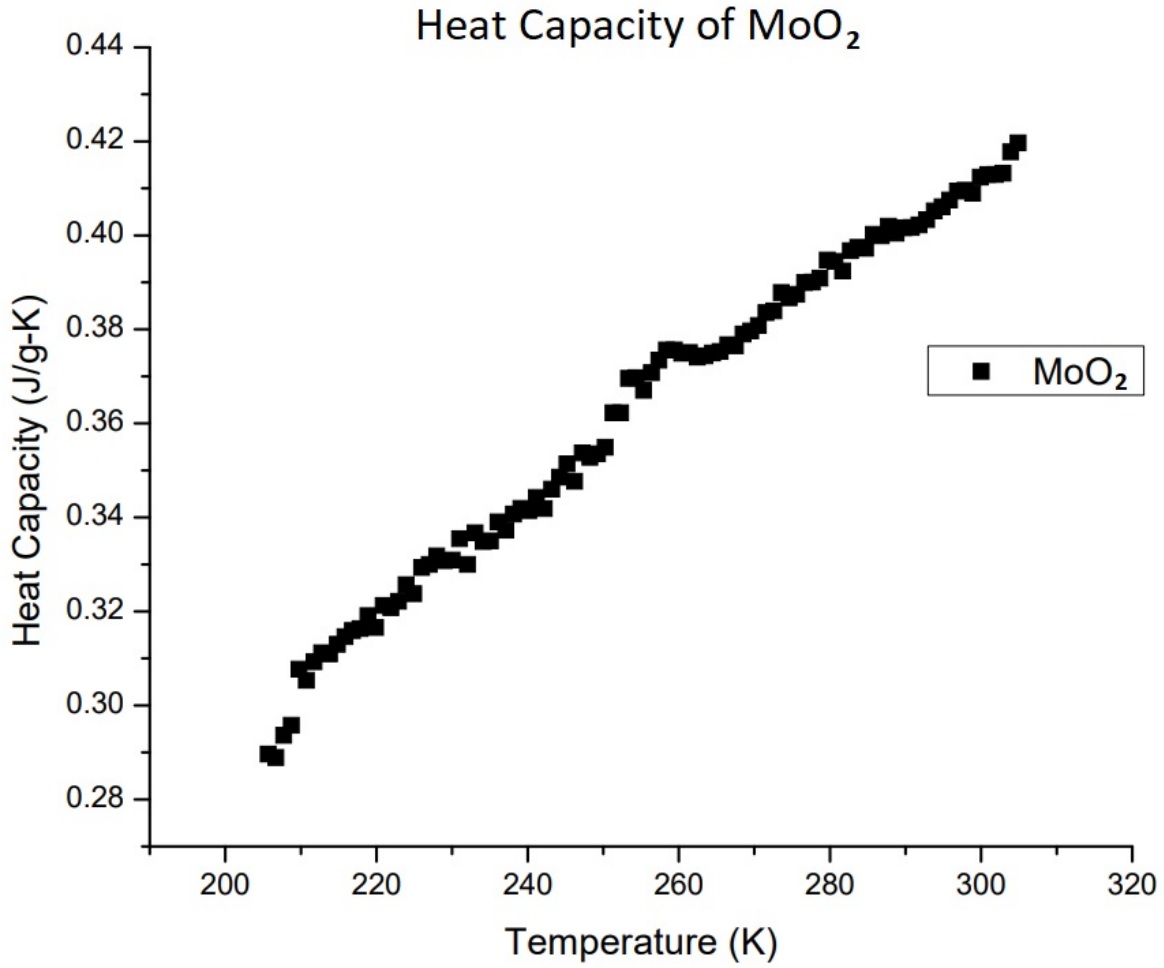


Figure 24: Heat Capacity of MoO<sub>2</sub> cooling from 300K to 200K.

Following the AC resistivity measurements, heat capacity measurements were performed to examine the behaviour around the 265K cooling and warming curve separation. A peak in the heat capacity can be seen forming around 263K and cresting at 259K, indicating that a transition is in fact occurring.

### 3.2.2 Anomalous Peak

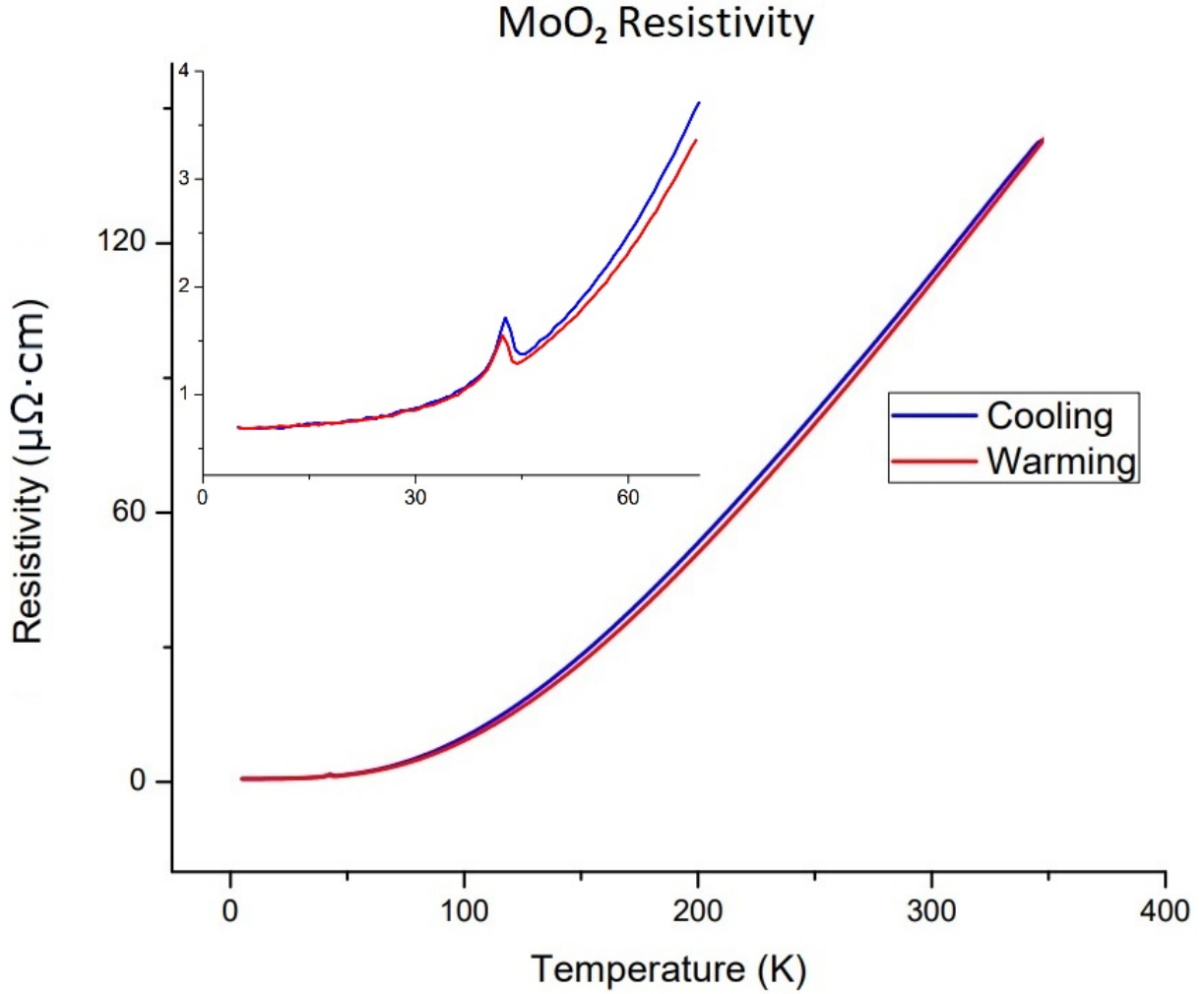


Figure 25: An unexpected peak in the resistivity of single crystal MoO<sub>2</sub> occurring at 43K with a 117Hz current.

Initially, AC resistivity measurements were performed at 117Hz, with results showing an unexpected peak at 43K. It was also observed that the peak is suppressed by an applied magnetic field. The peak was initially believed to be significant and further experiments around this temperature range were performed, the first to follow were DC measurements in the cryostat.



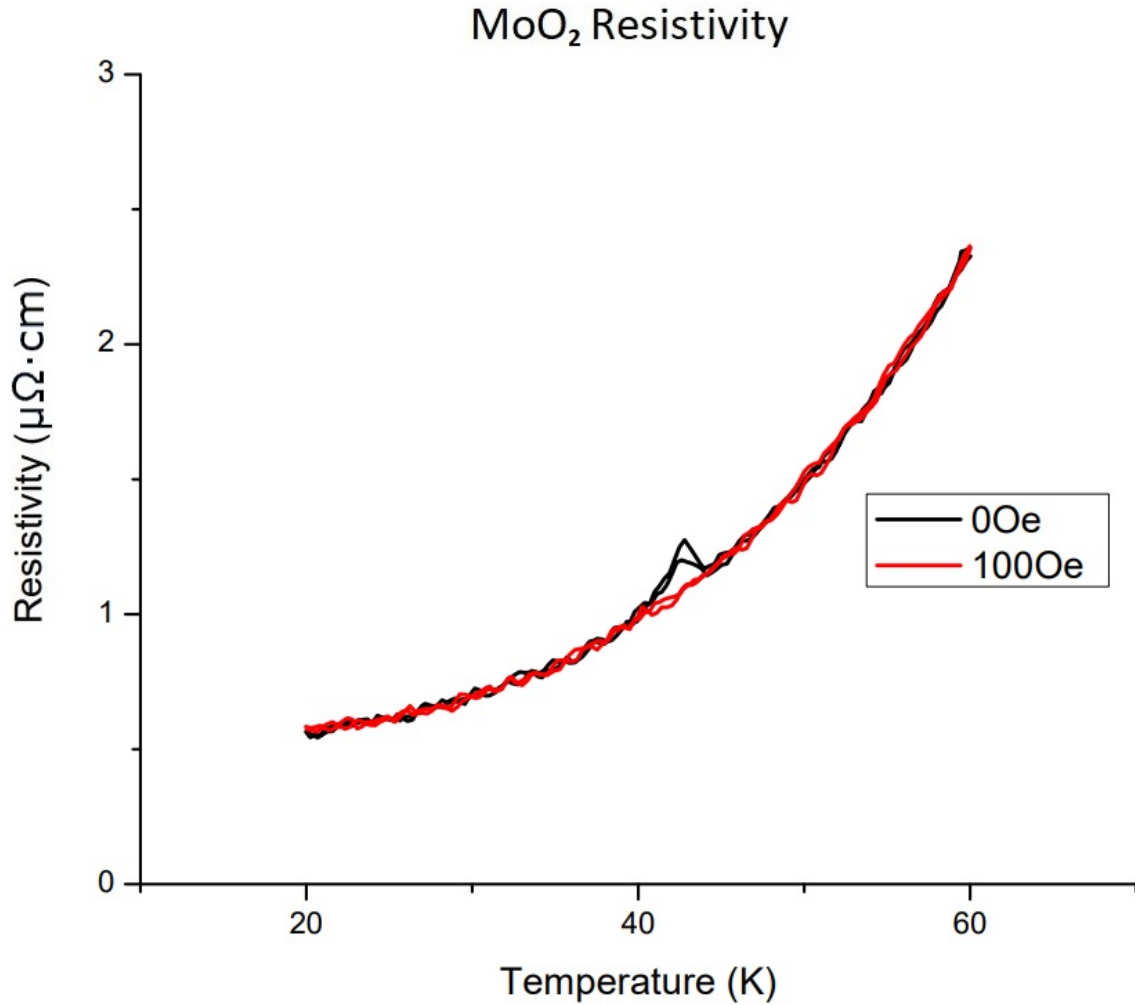


Figure 26: The 43K peak at 117Hz with no applied field and the peak being suppressed by a 100Oe applied magnetic field.

In figure 26 above, the presence and suppression of the 43K peak is shown. First the AC resistivity measurement is performed with no applied field in cooling and then warming, with the peak visible and unchanged by the direction of temperature change. Second, the same cooling and warming measurements were performed but now in a 100Oe applied magnetic field. Under the magnetic field the 43K peak is completely absent.

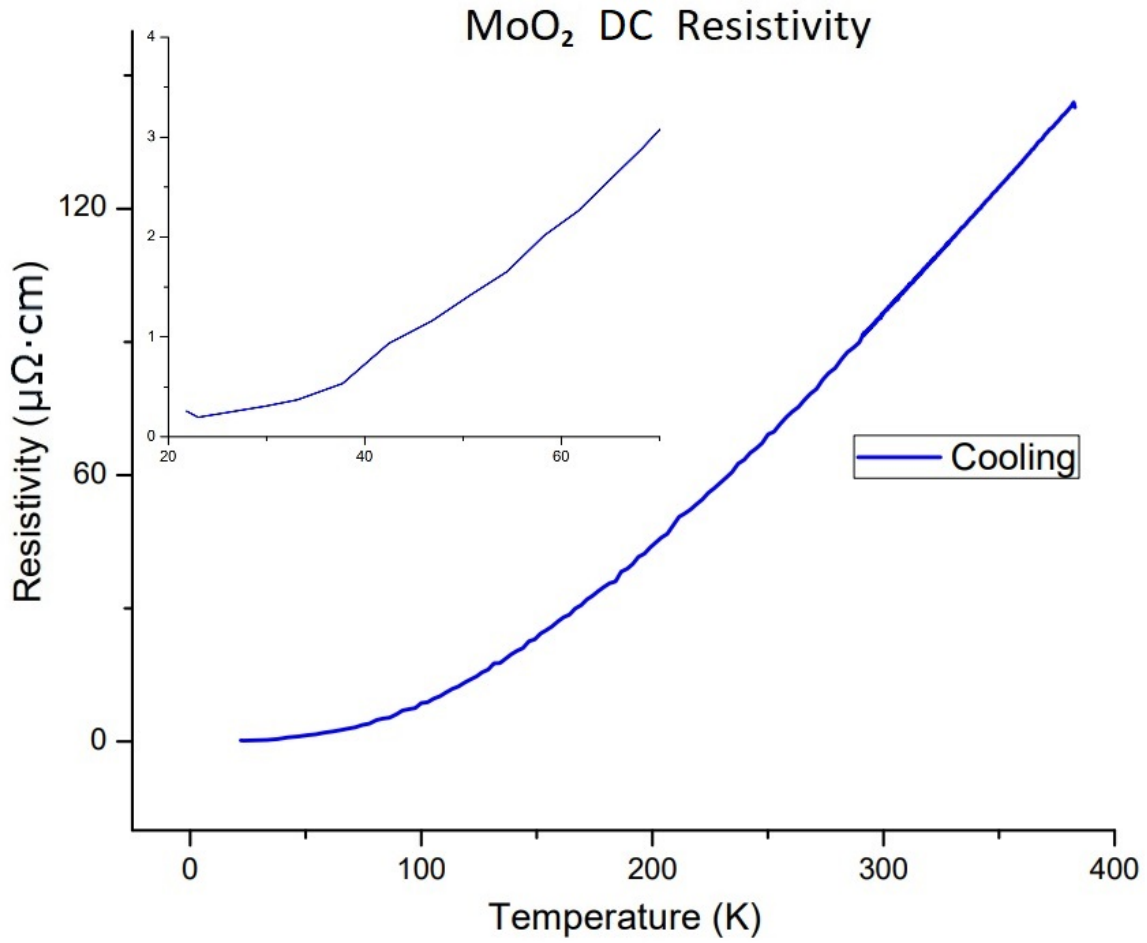


Figure 27: DC resistivity of  $\text{MoO}_2$  measured in the cryostat, with no peak at 43K apparent.

DC measurements performed on the single crystal  $\text{MoO}_2$  sample which had previously shown a peak at 43K, showed no evidence of a similar peak. Following this realization, it was determined that this now transient peak required further investigation.

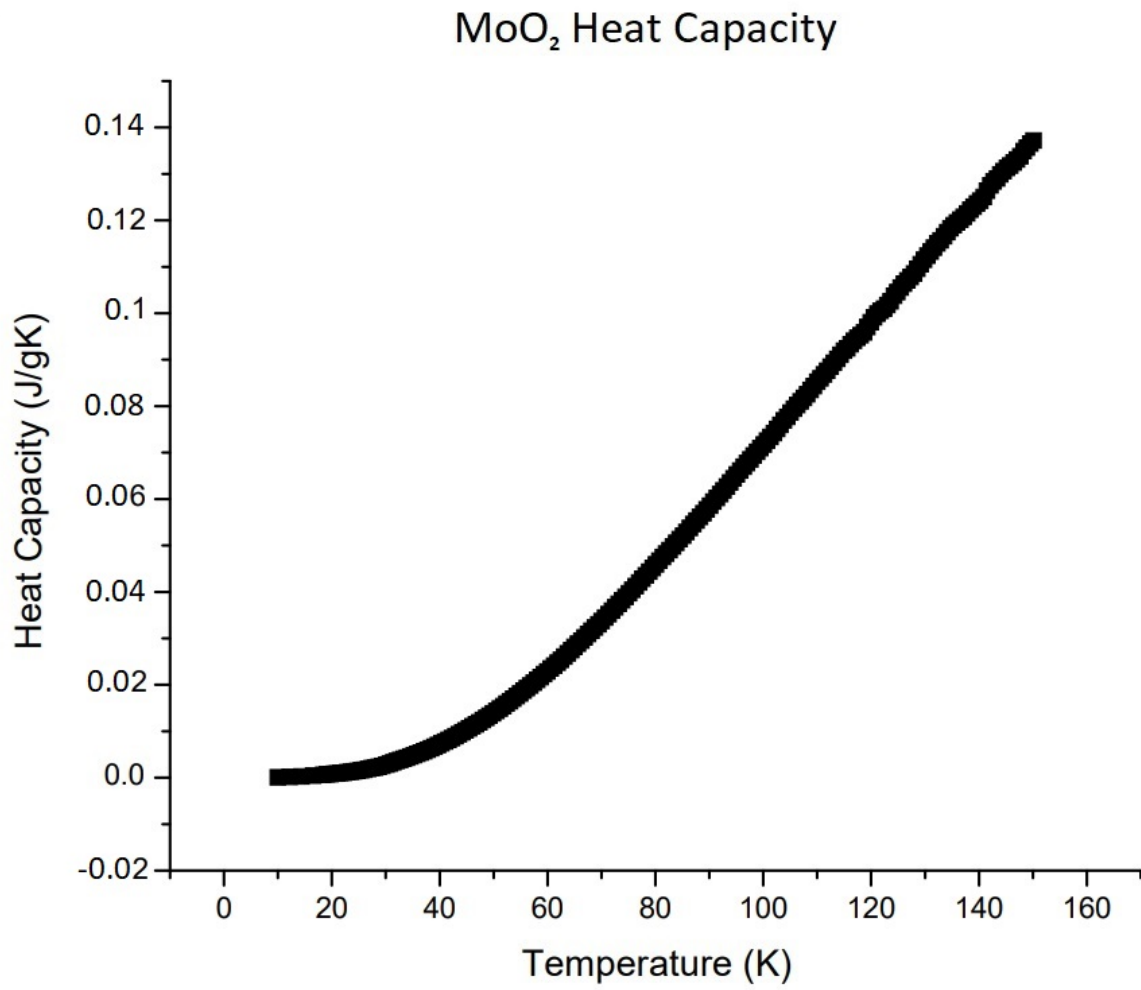


Figure 28: Results from 150K cooling down to 10K

The heat capacity exhibits no unusual behaviour at 43K, indicating that the cause of the AC resistivity peak is not a phase transition.

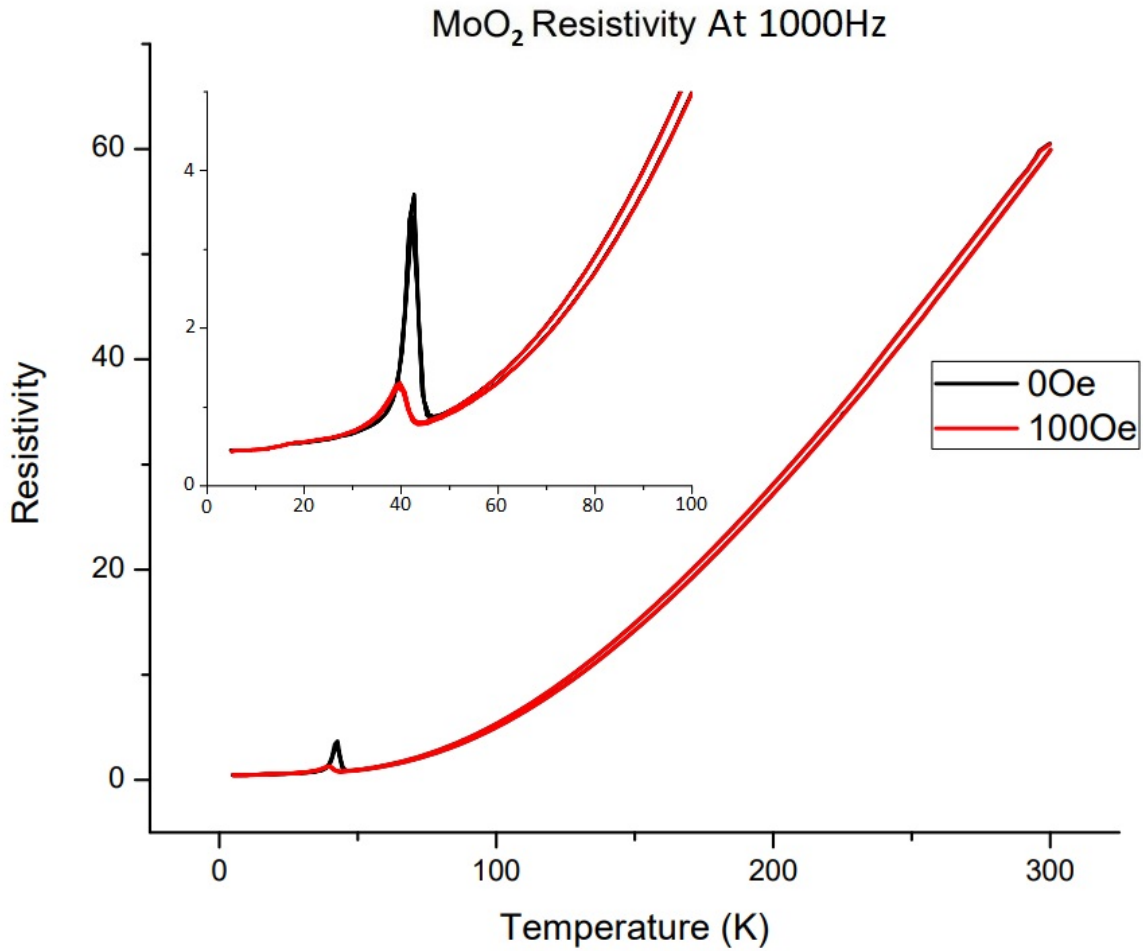


Figure 29: Resistivity of MoO<sub>2</sub> with 1000Hz AC with no magnetic field and with a 100Oe applied field.

Further investigation around this anomaly revealed that the peak was influenced by both the frequency of the current applied across the sample and the strength of the magnetic field. As frequency increases, so does the magnitude of the peak; as the magnetic field is increased the magnitude of the peak decreases while also shifting to lower temperature.

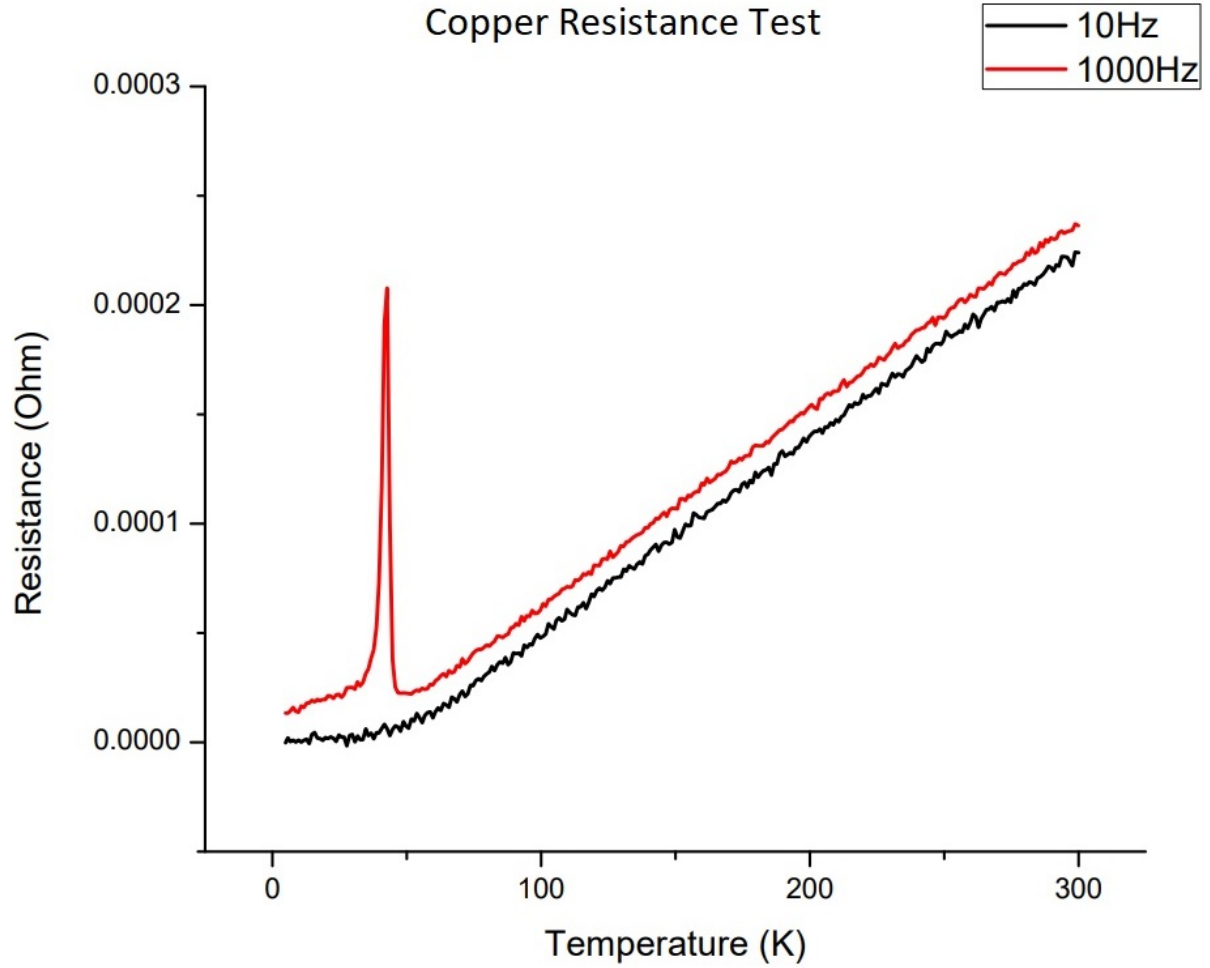


Figure 30: Resistance measurement of copper made on the PPMS showing the anomalous peak appearing at 43K.

In figure 30 the same 43K peak can be seen in measurements made on a copper strip, appearing only at elevated frequency. This indicated that the 43K peak is in fact an artefact of the measurement apparatus, appearing in low resistance samples when measured at high frequencies, and not a property of  $\text{MoO}_2$ .

### 3.3 TeCl<sub>4</sub> Growth

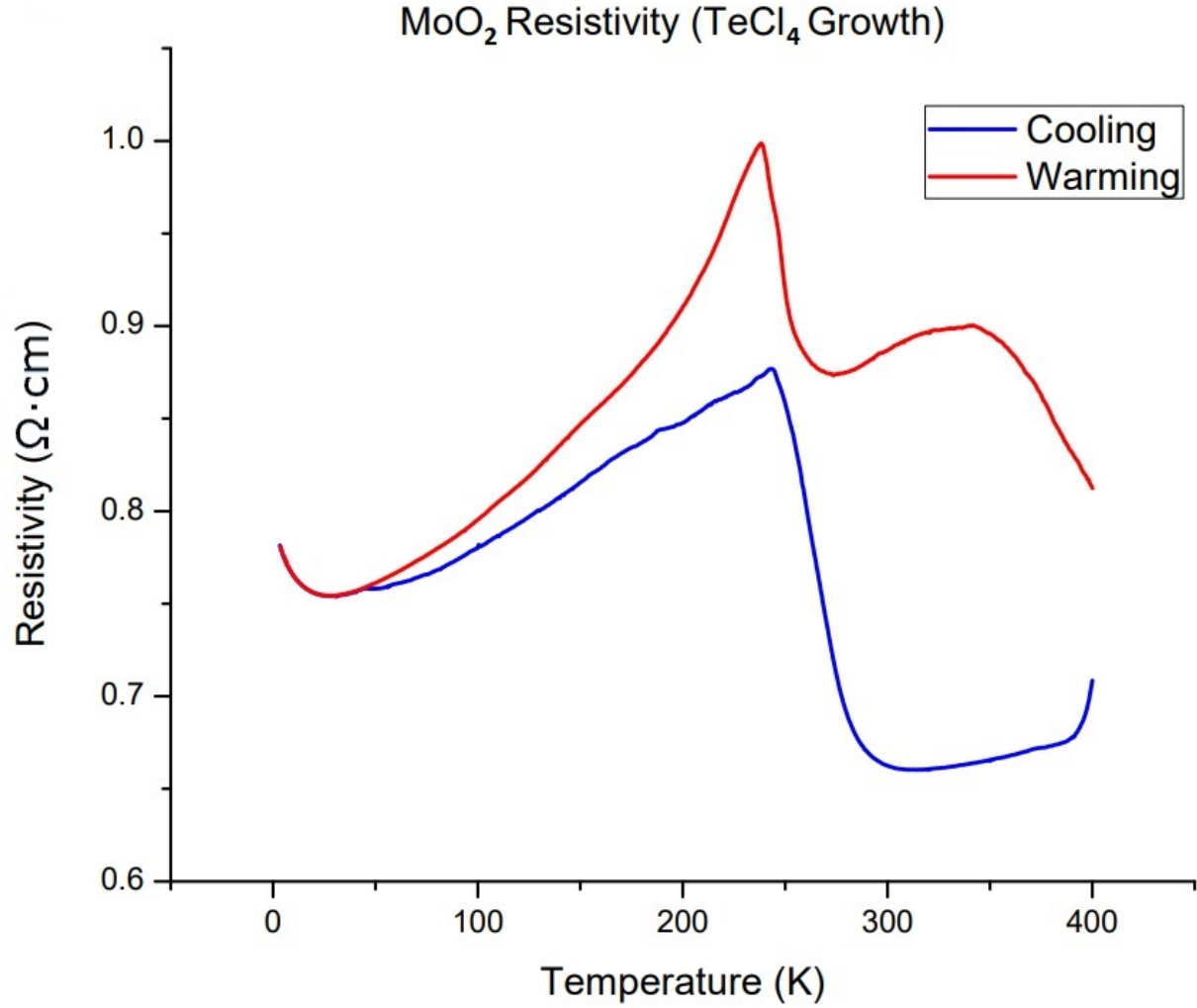


Figure 31: Resistivity of MoO<sub>x</sub> measured using QDPPMS, at 117Hz AC, sample is from TeCl<sub>4</sub> growth. Shows extensive hysteresis above 50K.

While appearing to be of acceptable quality on initial visual inspection, the crystals resulting from the TeCl<sub>4</sub> growths contained various contaminants. After growth a large crystal, roughly 3x3x5mm, was ground into a rectangular shape suitable for 4 probe resistivity measurements and analyzed. The result of this measurement, seen in figure 31, varied wildly from what was expected, based on previous MoO<sub>2</sub> results. The sample was cleaved, which can be seen in figure 9, revealing a mixture of compounds which were not

apparent externally. Powder diffraction confirmed that the sample was not homogeneous and was in fact a combination of  $\text{MoO}_2$ , two phases of  $\text{Mo}_9\text{O}_{26}$ , and  $\text{MoO}_3$ .

### 3.4 $\text{Mo}_4\text{O}_{11}$

The  $\text{Mo}_4\text{O}_{11}$  crystals found alongside the  $\text{MoO}_2$  crystals in the  $\text{I}_2$  sample growths were examined similarly.



Figure 32: Crystal showing its cleanest face left and the much rougher opposite face right.

Unfortunately, the rough face could not be ground entirely flat as doing so would have made the sample dangerously fragile. This resulted in deep grooves on one side which I expected to impact the magnitude of the resistivity. Heat capacity however, not being dependent on the cross section of the sample, should not be affected. Without performing single crystal diffraction on additional faces the orientation of the sample during resistivity measurements cannot be known with absolute certainty. However, given the results of the diffraction on the suitable face indicating it is in the (100) plane and the tendency of  $\text{Mo}_4\text{O}_{11}$  to grow longest along the b and c axes, all evidence indicates this is the axis along the b or c axis, or a combination of the two, though anisotropy between the two axes is minimal compared to the a-axis [14]. The samples produced were allowed to cool slowly below  $600^\circ\text{C}$ , meaning the expectation is that they will be in the  $\eta$  phase, as the high temperature  $\gamma$  phase is only stable at low temperatures when quenched to rapidly cool

below the transition temperature [14].

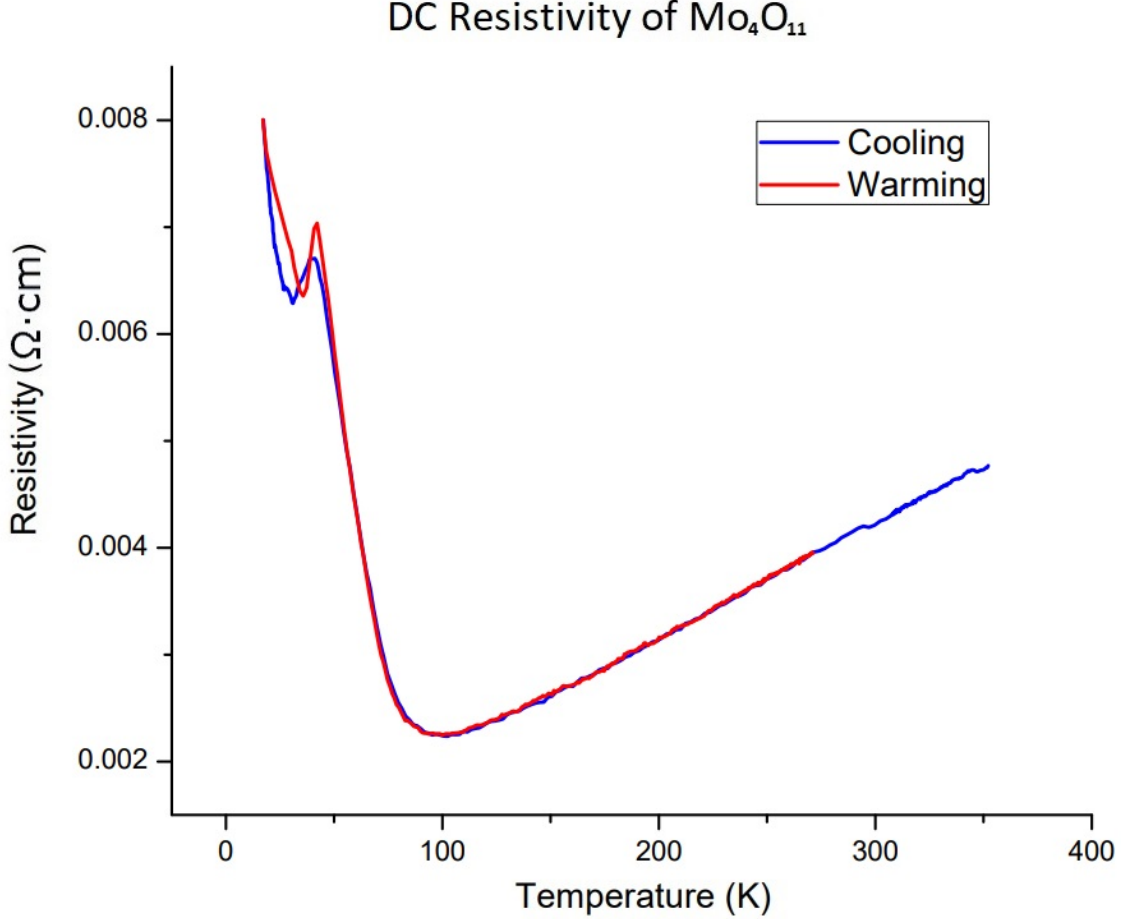


Figure 33: DC resistivity of  $\text{Mo}_4\text{O}_{11}$  cooling from 350K to 15K and warming to 275K.

DC resistivity measurements show transitions around the expected 109K and 30K [16] and some hysteresis in resistivity on warming up, until temperatures warm to  $\sim 50\text{K}$  above which the resistivity on cooling and warming match. Warming measurements were only taken up to room temperature due to difficulties getting the repaired heater to work reliably while simultaneously making resistivity measurements. These results, with the local minimal around 30K match the profile of  $\eta\text{-Mo}_4\text{O}_{11}$  as expected, since the sample was not heated above  $600^\circ\text{C}$  and quenched [17].



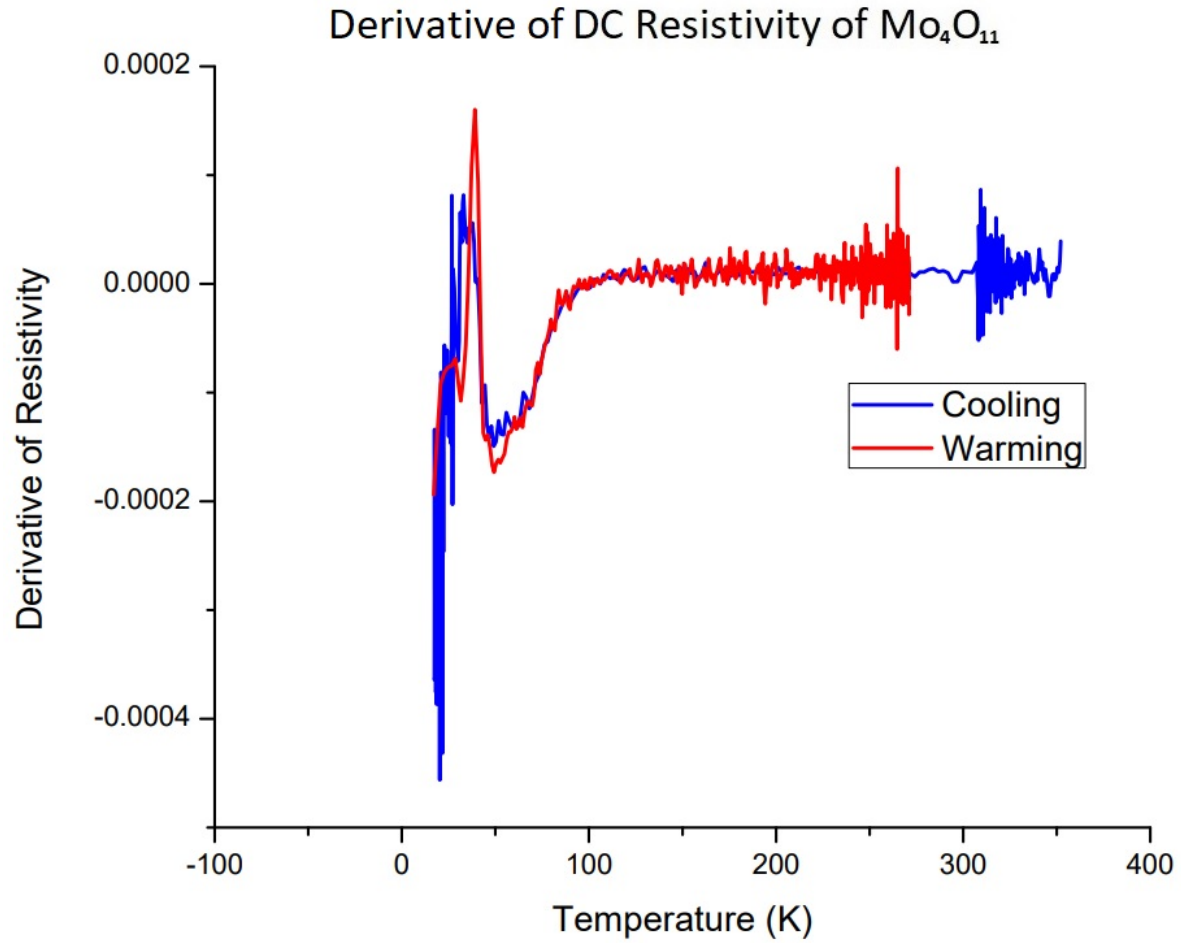


Figure 34: The derivative of the DC resistivity of  $\text{Mo}_4\text{O}_{11}$  cooling from 350K to 15K and warming to 275K.

The derivative of the DC resistivity shows the location of the peaks and the separation of the cooling and warming 25k peak.

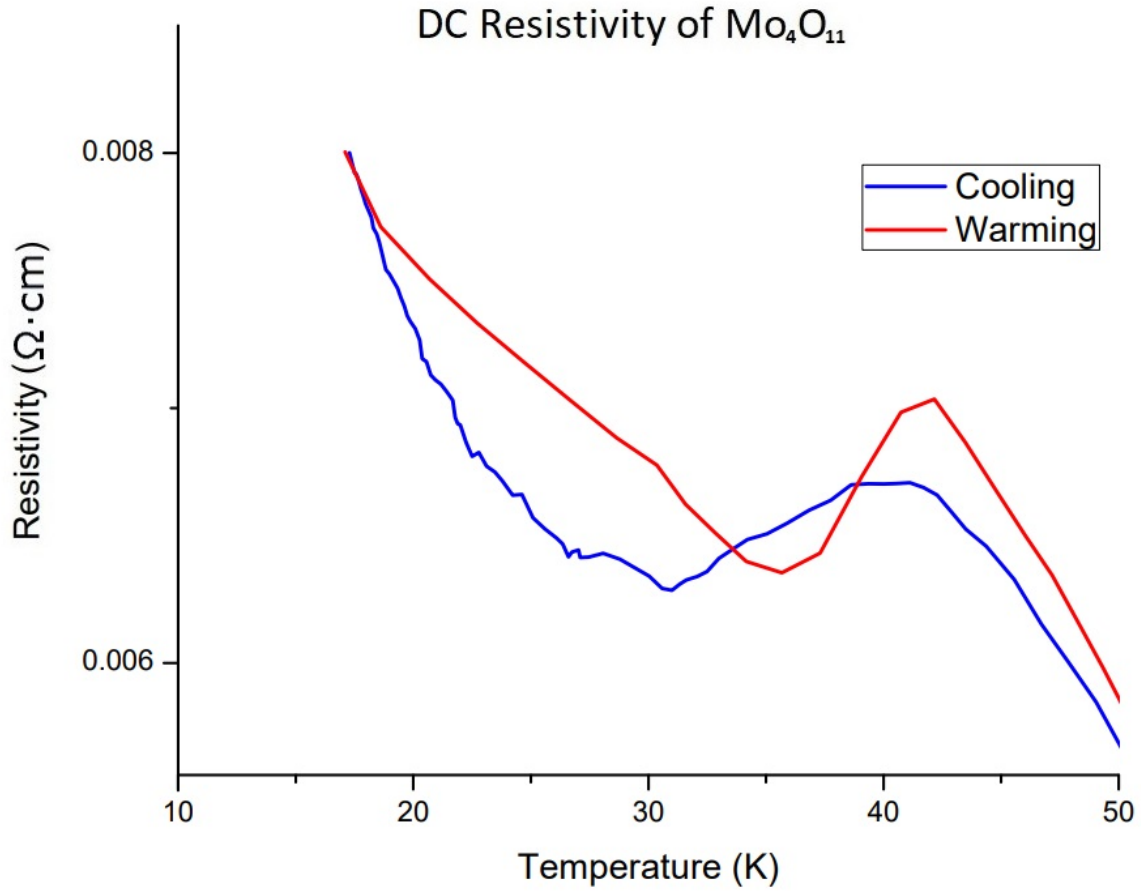


Figure 35: The DC resistivity of  $\text{Mo}_4\text{O}_{11}$  cooling from 350K to 15K and warming to 275K.

The 30K and 109K transitions can be seen clearly, however the reversal of the decreasing resistivity at 25K to again rise differs from the reports of other researches in which resistivity continues to fall [17].

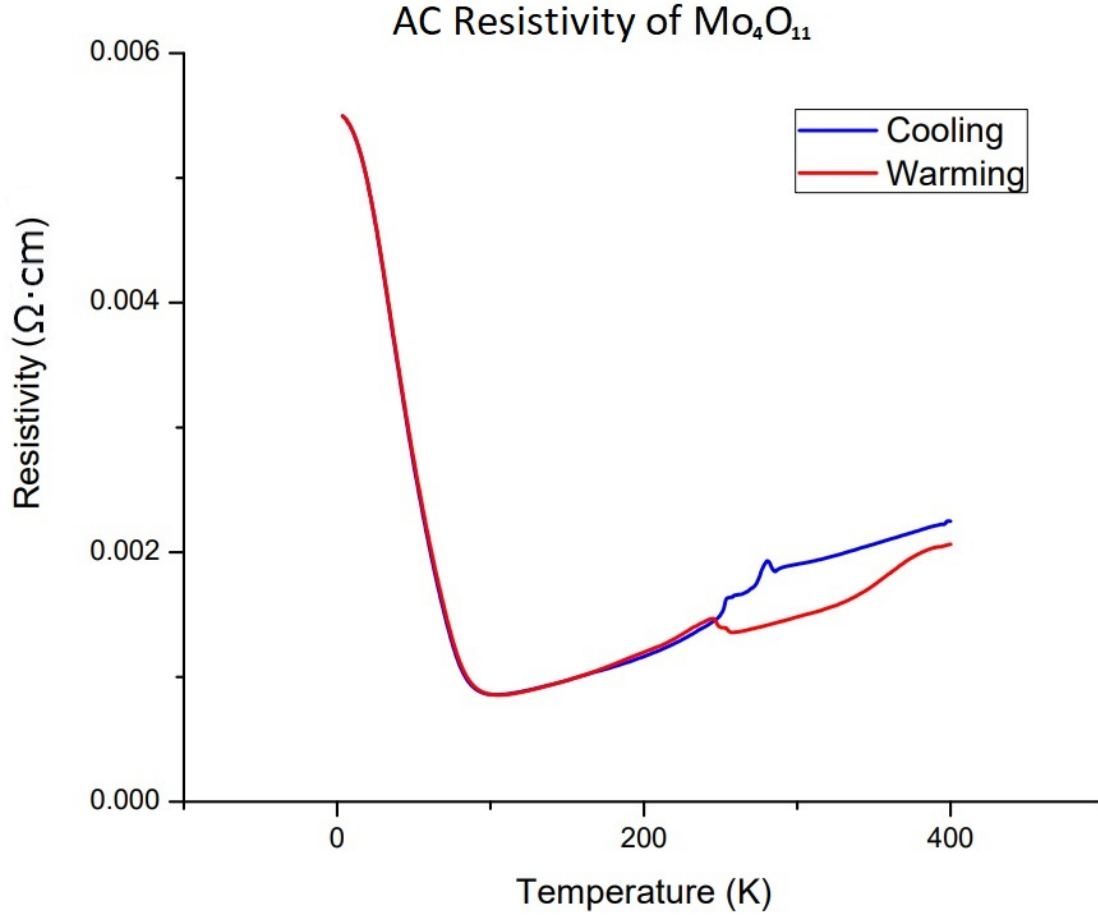


Figure 36: AC resistivity of  $\text{Mo}_4\text{O}_{11}$  between 400K and 3K at 117Hz.

AC resistivity measurements show largely similar behaviour between 50-250K with AC and DC measurements displaying unique features above and below this temperature range. The local minima and maxima below 50K present in the DC sample is completely absent in the AC measurement. The AC resistivity also shows none of the low temperature hysteresis seen in the DC measurements. New behaviours are also seen in the AC resistivity above 247K, at which point the warming and cooling curves diverge with the cooling curve increasing with increasing temperature and the warming curve decreasing. The cooling curve has two peaks at 254K and 281K, with a brief levelling off also seen in the warming

curve at 254K, though with no features as the sample warms through 281K. The lack of low temperature minima is unexpected, as based on resistivity alone, this would indicate that the sample is  $\gamma$ -Mo<sub>4</sub>O<sub>11</sub>.

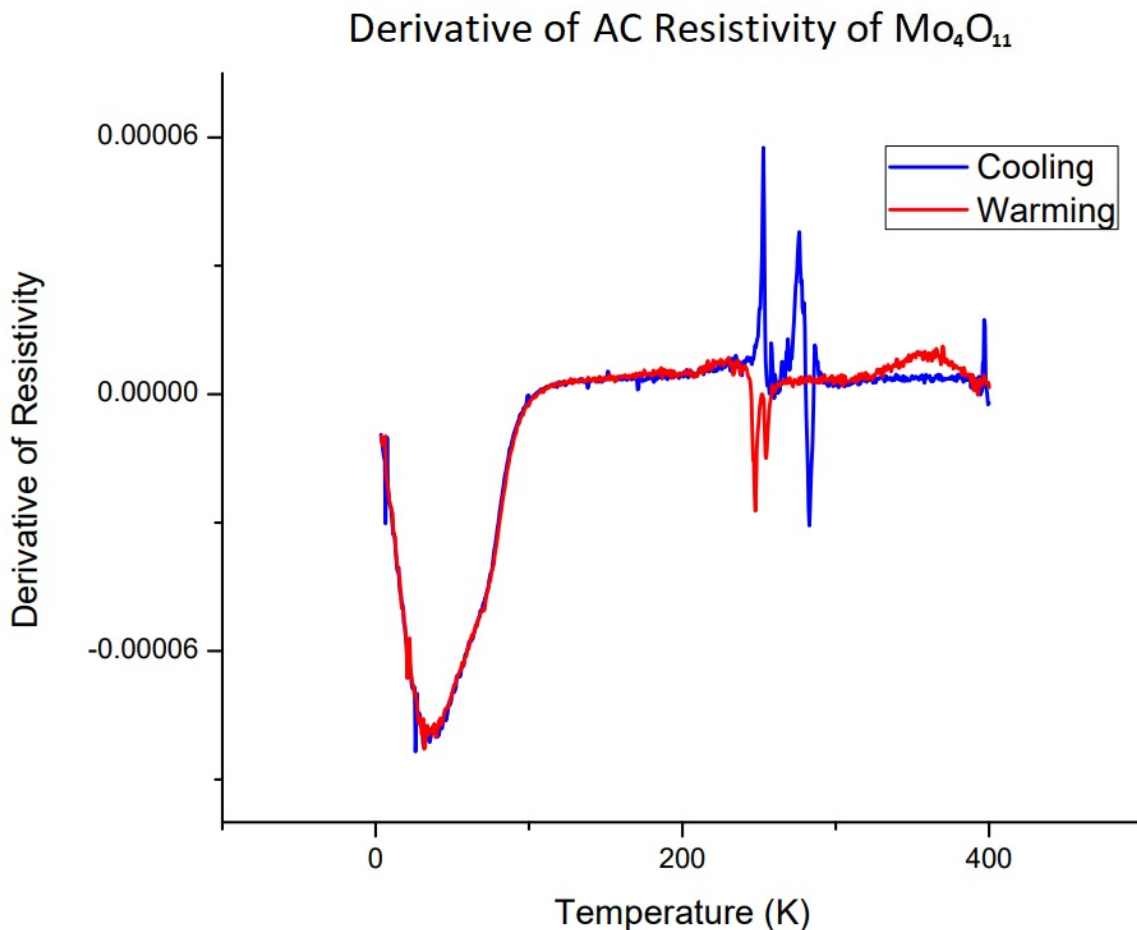


Figure 37: The derivative of the AC resistivity of Mo<sub>4</sub>O<sub>11</sub> between 400K and 3K at 117Hz.

In addition to the established 109K and 30K transitions reported in  $\eta$ -Mo<sub>4</sub>O<sub>11</sub> and at 95K in  $\gamma$ -Mo<sub>4</sub>O<sub>11</sub>, features can be seen with added clarity at 247K, 254K, 281K, 286K, and potentially 375K.

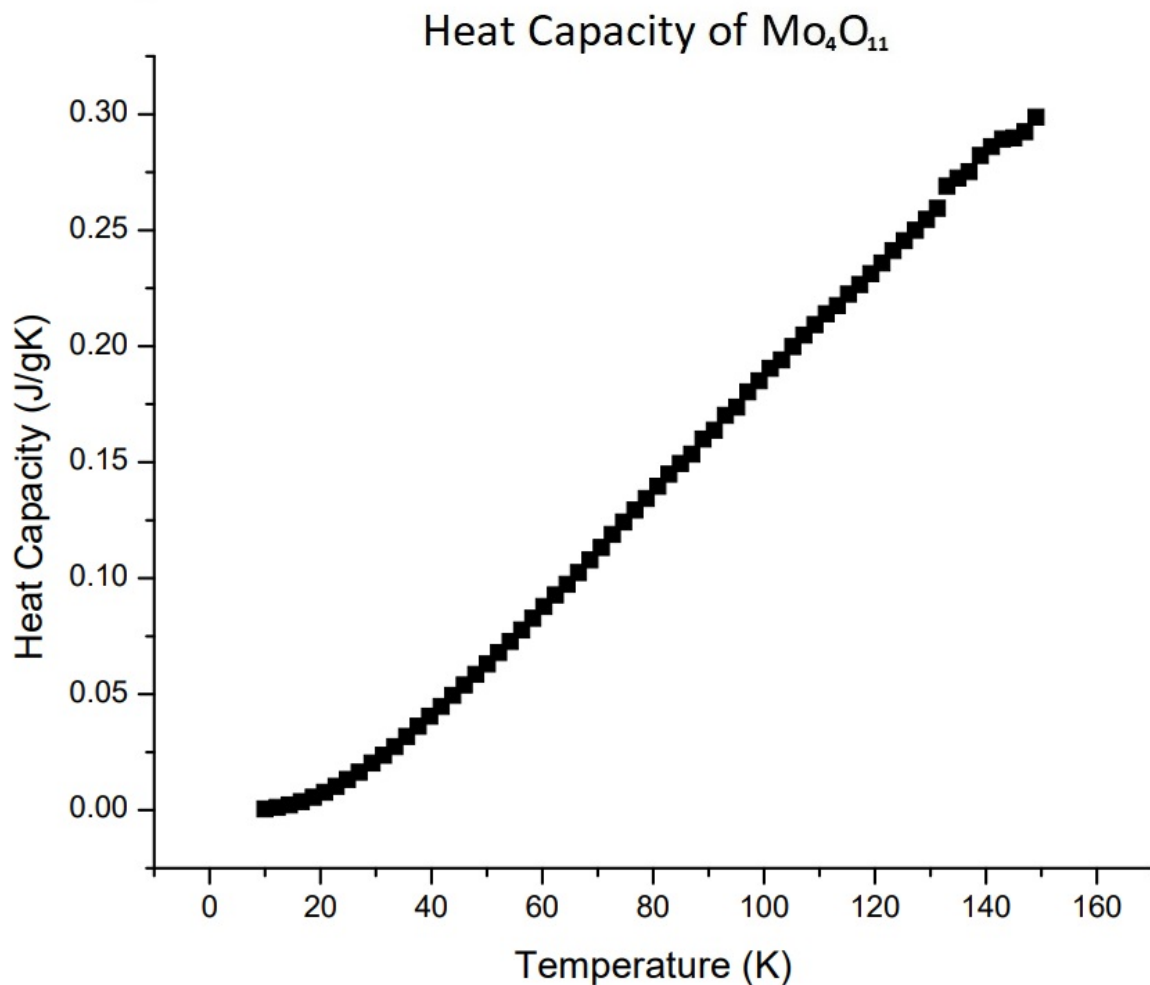


Figure 38: Heat capacity of  $\text{Mo}_4\text{O}_{11}$  cooling from 150K to 10K.

While the resistive properties of  $\text{Mo}_4\text{O}_{11}$  change rapidly at 109K, no evidence of a transition is observed in the heat capacity. This matches results reported by Schlenker et. al. where the 100K transition was not apparent in heat capacity measurements [17]. The low temperature peak and trough seen below 30K in figure 34 do not present as features in the heat capacity either.

## 4 Discussion and Conclusion

### 4.1 Crystal Growth and Transport Ions

Growths using  $I_2$  as the transport agent were the most successful, with source and growth zone temperatures of  $900^\circ\text{C}$  and  $700^\circ\text{C}$  producing the most consistent results. The size and shape of crystals in  $I_2$  growths was consistent over the range of successful temperatures, though the quantity of  $I_2$  had a significant effect, with crystal size and growth time being inversely proportional to the availability of transport ions. When attempts to lower growth zone temperature were made the growth zone would expand, climbing up the temperature gradient, if the temperature was raised the growth zone shrank towards the far end of the ampule where temperature was lowest. However at no point did excessive temperature prevent growth outright. When temperatures were too high it appeared that all growth would occur rapidly when the ampule was cooling. In the few cases where higher temperature growth was tried, the total crystal production seemed to be directly proportional to the amount  $I_2$  available and independent of growth time. Unfortunately crystals produced under these conditions were too small for any measurements other than powder diffraction.

$\text{TeCl}_4$  growths were also performed with moderate success producing larger crystals than  $I_2$  in less time. Unfortunately, this procedure invariably resulted in crystals of an inferior quality. Twinning was extensive in larger crystals, as were internal voids which only became apparent upon cleaving of samples. Similar to some of the  $I_2$  growths, a fraction of the product was molybdenum oxides other than  $\text{MoO}_2$ . Unlike in the  $I_2$  growths,  $\text{TeCl}_4$  growths produced crystals where multiple different oxides had grown together. These intertwined crystals were exceedingly difficult to separate, and attempts to do so resulted in crystals no larger than those grown using  $I_2$  and whose quality remained questionable.

One growth attempt was made using bromine which had been solidified in liquid nitrogen and was performed under the same conditions as the growths using  $I_2$ . However,

this ampule ruptured and further efforts were not made with this transport agent, due to the high volatility of bromine and the difficulties it presented relative to solid transport ion sources. Molybdenum bromide was then considered, having a suitable decomposition temperature and not introducing any unnecessary elements make it an attractive potential transport ion donor. However by this time acceptable samples had already been produced and the idea was not pursued further.

## 4.2 MoO<sub>2</sub> Features and Transitions

In MoO<sub>2</sub> single crystals grown by CVT with TeCl<sub>4</sub> decomposing to provide Cl transport ions, transitions at 267K and 220K were reported . These transitions were identified based on measurements of resistivity, heat capacity, and thermal expansion [1].

In the I<sub>2</sub> grown crystals, upon which resistivity and heat capacity measurements were made, both the resistivity measurements, clarified by examining the derivative of the resistivity, and the heat capacity measurements supported the existence of a 267K transition. When warming above 267K the AC resistivity begins to deviate from the resistivity measured during cooling, as seen in figure 22. The derivatives of these two curves show signs of a transition around the 267K on cooling of the sample which appears again at roughly 360K when heating up, evidenced by figure 23. However, evidence of a transition at 220K was not apparent. None of the measurements performed on I<sub>2</sub> grown MoO<sub>2</sub> single crystals indicated that such a transition was present.

The 43K peak was first observed during 117Hz AC resistivity measurements in the QDPPMS. Neither resistivity measurements made using the DC cryostat nor results of heat capacity measurements showed any evidence of a 43K peak. The peak was frequency dependent, reaching a maximum at the PPMS's limit of 1000Hz and could be suppressed by an applied magnetic field on the order of 100Oe. Measurements were performed using different resistivity pucks to eliminate this possible source of error, to no avail. Ultimately,

testing was done with a copper strip shown in figure 30, which showed an identically located peak of similar magnitude and magnetic field dependence. It was thus concluded that this peak was an artifact of the measurement apparatus which appeared in low resistance samples at high frequency and was not a property of the  $\text{MoO}_2$  sample itself.

### 4.3 $\text{Mo}_4\text{O}_{11}$

The appearance of  $\text{Mo}_4\text{O}_{11}$  single crystals in some of the  $\text{MoO}_2$  growths made it possible to examine an additional molybdenum oxide without needing to deduce another set of growth conditions. These  $\text{Mo}_4\text{O}_{11}$  crystals were first identified using powder diffraction, in the same way that the identity of the  $\text{MoO}_2$  crystals had been confirmed. AC and DC resistivity measurements showed similar general behaviour, in particular a minimum around 100K corresponding to the established 109K, and in the AC measurement possibly the  $\gamma$  phase 95K CDW transitions. The presence of other features varied between measurement apparatus. In the DC cryostat a local minima and maxima were present, behaviour which corresponds to a 30K CDW transition, though this feature was entirely absent in measurements made using the PPMS. While the same sample was used for each measurement and it was never heated to the transition point, the difference between AC and DC measurements, particularly around the 30K maxima and minima, appear to mirror the difference between  $\eta\text{-Mo}_4\text{O}_{11}$  and  $\gamma\text{-Mo}_4\text{O}_{11}$  [17]. The AC measurements on the PPMS also showed features not seen in the DC resistivity, but in the high temperature range. Between 200K and 400K a significant hysteresis was observed, with two sharp peaks present in the cooling regime at 250K and 285K. Analysis of the derivatives of the AC and DC curves show that the high temperature peaks are unique to the AC measurements and persisted across multiple measurements. Heat capacity measurements performed from 150-10K showed no features at the 109K and 30K transition temperatures as expected, although the high temperature behaviour warrants further investigation.



## References

- [1] Leandro Alves, Felipe Oliveira, Bruno de Lima, Mario da Luz, A. Rebello, Sueli Masunaga, J.J. Neumeier, C. Giles, Juscelino Leao, and C. dos Santos. Evidence of phase transitions in moo2 single crystals. *Journal of Alloys and Compounds*, 705, 02 2017.
- [2] Compiled by A. D. McNaught and B. Kosata; updates compiled by A. Jenkins A. Wilkinson created by M. Nic, J. Jirat. *IUPAC. Compendium of Chemical Terminology, 2nd ed. (the "Gold Book") "transition element"*. Blackwell Scientific Publications, Oxford (1997), 1995.
- [3] P. S. Matsumoto. Trends in Ionization Energy of Transition-Metal Elements. *Journal of Chemical Education*, 82:1660, November 2005.
- [4] P. A. Cox. *Transition Metal Oxides. An Introduction to Their Electronic Structure and Properties*. Oxford University Press, 2010.
- [5] R. Tokarz-Sobieraj and M. Witko. (2007). Electronic Properties of the Active Sites Present at the (011) Surface of MoO<sub>2</sub>. *Adsorption Science Technology*, 25(8), 583596. <https://doi.org/10.1260/0263-6174.25.8.583>.
- [6] Björn G. Brandt and A. C. Skapski. A refinement of the crystal structure of molybdenum dioxide. *Acta Chemica Scandinavica*, 21:138–143, 1967.
- [7] Malgorzata Witko Renata Tokarz-Sobieraj, Robert Grybos. Electronic structure of moo2. dft periodic and cluster model studies. *Applied Catalysis A: General*, page 137143, 01 2011.
- [8] Y. Shimony L. Ben-Dor. Crystal structure, magnetic susceptibility and electrical conductivity of pure and nio-doped moo<sub>2</sub> and wo<sub>2</sub>. *Hebrew University, Jerusalem*, 1974.

- [9] William H. McCarroll Kandalam V. Ramanujachary. Oxides: Solid-state chemistry. page 28, 2006.
- [10] L.M.S. Alves C.A.M. dos Santos R.J.O. Mossaneck V. Stoeberl, M. Abbate. X-ray spectroscopy and electronic structure of  $\text{moO}_2$ . *Journal of Alloys and Compounds*, 691:138–143, 2017.
- [11] Byeong Wan Kwon Jinsoo Kim M. Grant Norton Su Ha Xiaoxue Hou, Oscar Marin-Flores. Gasoline-fueled solid oxide fuel cell using  $\text{moO}_2$ -based anode. *Journal of Power Sources*, 268:546–549, 2014.
- [12] Joe Breiter Jinsoo Kim M. Grant Norton Su Ha Byeong Wan Kwona, Caleb Ellefsonb. Molybdenum dioxide-based anode for solid oxide fuel cell applications. 243:203–210, 2013.
- [13] Stig Åsbrink and Lars Kihlberg. A study of the crystal symmetry and structure of orthorhombic  $\text{mo}_4\text{O}_{11}$  by least-squares techniques. *Acta Chem. Scand.*, 18:1571–1573, 1964.
- [14] M. S. da Luz, A. de Campos, B. D. White, and J. J. Neumeier. Electrical resistivity, high-resolution thermal expansion, and heat capacity measurements of the charge-density wave compound  $\gamma\text{-mo}_4\text{O}_{11}$ . *Phys. Rev. B*, 79:233106, Jun 2009.
- [15] L. Kihlberg. Crystal structure studies on monoclinic and orthorhombic  $\text{mo}_4\text{O}_{11}$ . *Arkiv för Kemi*, 21:365–377, 1963.
- [16] H Guyot et al. Charge density wave instabilities in the quasi-two dimensional metal  $\text{-mo}_4\text{O}_{11}$ . *J. Phys. C: Solid State Phys.*, 16:1227–1232, 1983.

- [17] C. Escribe-Filippini H. Guyot J. Marcus C. Schlenker, J. Dumas and G. Fourcaudot. Charge-density-wave instabilities in the low-dimensional molybdenum bronzes and oxides. *Philosophical Magazine B*, 52:643–667, 03 1985.
- [18] Haibin Zhu-Guangyan Liu Libin Sun Li Shi Han Jiang Shaopeng Ma Xiaojuan Zhang, Yanan Yi. Measurement of tensile strength of nuclear graphite based on ring compression test. *Journal of Nuclear Materials*, pages 134–140, September 2018.
- [19] I.M. Mikhailovskij T.I. Mazilova, E.V. Sadanov. Tensile strength of graphene nanoribbons: An experimental approach. *Materials Letters*, pages 17–19, January 2019.
- [20] Michael Fowler. Electrons in one dimension: the peierls transition. <http://galileo.phys.virginia.edu/classes/752.mf1i.spring03/PeierlsTrans.htm> (19/11/22), February 2007.
- [21] H.K.D.H. Bhadeshia and C.M. Wayman. 9 - phase transformations: Nondiffusive. In David E. Laughlin and Kazuhiro Hono, editors, *Physical Metallurgy (Fifth Edition)*, pages 1021 – 1072. Elsevier, Oxford, fifth edition edition, 2014.
- [22] 6E McGraw-Hill Dictionary of Scientific Technical Terms. Iodine process. <https://encyclopedia2.thefreedictionary.com/Iodide+Process>, August 2019.
- [23] Robert Glaum Peer Schmidt, Michael Binnewies and Modeling Advanced Topics on Crystal Growth Sukarno Olavo Ferreira IntechOpen DOI: 10.5772/55547. Available from: <https://www.intechopen.com/books/advanced-topics-on-crystal-growth/chemical-vapor-transport-reactions-methods-materials-modeling> Marcus Schmidt (February 20th 2013). Chemical Vapor Transport ReactionsMethods, Materials.

- [24] Von H. Oppermann. Beitrge zur chemie der oxidhalogenide von molybden und wolfram. iv. der transport von  $\text{MoO}_2$  mit  $\text{J}_2$  und die existenz von  $\text{MoO}_2\text{J}_2$ . *Zeitschrift fr anorganische und allgemeine Chemie, Wiley Online Library*, 1971.
- [25] Quantum Design. *Physical Property Measurement System Heat Capacity Option Users Manual 11th edition*. Quantum Design, 2004.
- [26] T. Sekiya. Flux growth of  $\text{MoO}_2$  single crystals. *Materials Research Bulletin*, 16:841–846, April 1981.
- [27] Yasutoshi Kato Yoshichika Bando and Toshio Takada. Crystal growth of molybdenum oxides by chemical transport. *Bulletin of the Institute for Chemical Research, Kyoto University*, December 1976.

# A Appendix

Table A.1: MoO<sub>2</sub> Diffraction Peak List

MoO <sub>2</sub> Diffraction Peaks		
h,k,l	Observed Peak	Ideal Peak
1,0,0	18.42647°	18.43628°
1,1,-1	25.83312°	25.84292°
0,1,1	25.99868°	26.00849°
1,1,0	26.04374°	26.05355°
1,0,-2	31.78559°	31.7954°
2,0,-2	36.7513°	36.76111°
1,1,-2	36.89416°	36.90397°
0,2,0	36.97147°	36.98128°
2,1,-1	36.99284°	37.00265°
0,0,2	37.23241°	37.24222°
1,1,1	37.35217°	37.36197°
2,0,0	37.36291°	37.37272°
2,1,-2	41.3265°	41.33631°
1,2,-1	41.47629°	41.48609°
0,2,1	41.58544°	41.59525°
1,2,0	41.61522°	41.62503°
0,1,2	41.763°	41.77281°
2,1,0	41.88159°	41.8914°
3,0,-2	49.47178°	49.48159°
1,2,-2	49.54148°	49.55129°

MoO <sub>2</sub> Diffraction Peaks		
h,k,l	Observed Peak	Ideal Peak
2,2,-1	49.61939°	49.6292°
1,2,1	49.90382°	49.91363°
1,0,2	50.22929°	50.2391°
2,1,-3	53.03961°	53.04942°
2,2,-2	53.12245°	53.13226°
3,1,-2	53.16323°	53.17304°
1,1,-3	53.31087°	53.32068°
0,2,2	53.48353°	53.49334°
3,1,-1	53.50786°	53.51767°
2,2,0	53.58187°	53.59168°
1,1,2	53.88332°	53.89313°
2,1,1	53.95671°	53.96652°
3,0,0	57.43693°	57.44674°
3,1,-3	59.84003°	59.84984°
1,3,-1	60.14511°	60.15492°
0,3,1	60.22853°	60.23834°
1,3,0	60.2513°	60.26111°
0,1,3	60.5906°	60.60041°
3,1,0	60.79467°	60.80448°
2,2,-3	63.23047°	63.24028°
3,2,-2	63.34114°	63.35095°
1,2,-3	63.47342°	63.48322°
3,2,-1	63.65007°	63.65988°
1,2,2	63.98725°	63.99706°

MoO <sub>2</sub> Diffraction Peaks		
h,k,l	Observed Peak	Ideal Peak
2,2,1	64.05323°	64.06304°
2,0,-4	66.42826°	66.43806°
1,3,-2	66.58024°	66.59005°
2,3,-1	66.64487°	66.65468°
4,0,-2	66.68687°	66.69668°
1,3,1	66.88118°	66.89099°
2,0,2	67.62937°	67.63918°
3,0,-4	69.29051°	69.30032°
3,2,-3	69.41771°	69.42752°
2,1,-4	69.53662°	69.54643°
2,3,-2	69.59399°	69.6038°
4,1,-2	69.78967°	69.79948°
0,3,2	69.9026°	69.9124°
1,0,-4	69.90832°	69.91813°
2,3,0	69.98679°	69.9966°
0,2,3	70.11201°	70.12181°
3,2,0	70.30113°	70.31094°
2,1,2	70.71255°	70.72236°
3,1,-4	72.34163°	72.35144°
4,1,-3	72.48682°	72.49663°
1,1,-4	72.94831°	72.95812°
4,1,-1	73.25829°	73.2681°
1,1,3	73.62187°	73.63168°
3,1,1	73.78667°	73.79648°

MoO <sub>2</sub> Diffraction Peaks		
h,k,l	Observed Peak	Ideal Peak
4,0,-4	78.18698°	78.19678°
2,3,-3	78.52398°	78.53378°
2,2,-4	78.53671°	78.54652°
3,3,-2	78.62484°	78.63465°
0,4,0	78.72629°	78.7361°
1,3,-3	78.74547°	78.75528°
4,2,-2	78.77872°	78.78852°
3,3,-1	78.90671°	78.91652°
1,3,2	79.21492°	79.22473°
2,3,1	79.2753°	79.28511°
0,0,4	79.36772°	79.37753°
2,2,2	79.66294°	79.67275°
4,0,0	79.68945°	79.69926°
4,1,-4	81.11637°	81.12618°
3,2,-4	81.22985°	81.23966°
4,2,-3	81.36988°	81.37969°
1,4,-1	81.61743°	81.62724°
0,4,1	81.69059°	81.7004°
1,4,0	81.71057°	81.72038°
1,2,-4	81.81533°	81.82514°
4,2,-1	82.11487°	82.12468°
0,1,4	82.2868°	82.29661°
1,2,3	82.46656°	82.47637°
4,1,0	82.60595°	82.61575°



MoO <sub>2</sub> Diffraction Peaks		
h,k,l	Observed Peak	Ideal Peak
3,2,1	82.6261°	82.6359°
3,3,-3	84.25493°	84.26474°
0,3,3	84.90933°	84.91914°
3,3,0	85.08797°	85.09778°
1,4,-2	87.39591°	87.40571°
2,4,-1	87.45529°	87.46509°
1,4,1	87.67264°	87.68245°
5,0,-2	87.76329°	87.77309°
3,0,2	88.92197°	88.93178°
4,2,-4	89.79636°	89.80616°
3,1,-5	89.86818°	89.87799°

Table A.2: Mo<sub>4</sub>O<sub>11</sub> Diffraction Peak List

Mo <sub>4</sub> O <sub>11</sub> Diffraction Peaks		
h,k,l	Observed Peak	Ideal Peak
1,0,1	13.57054°	13.59773°
4,0,0	14.43724°	14.46443°
2,0,1	14.95037°	14.97756°
3,0,1	17.00863°	17.03583°
2,1,0	17.75876°	17.78596°
4,0,1	19.53916°	19.56636°
0,1,1	20.89279°	20.91999°
1,1,1	21.20841°	21.23561°
6,0,0	21.7426°	21.7698°
4,1,0	21.78119°	21.80839°
2,1,1	22.12953°	22.15673°
5,0,1	22.39105°	22.41825°
3,1,1	23.58889°	23.61608°
6,0,1	25.46647°	25.49367°
4,1,1	25.49974°	25.52693°
0,0,2	26.36072°	26.38791°
1,0,2	26.61497°	26.64217°
6,1,0	27.24871°	27.2759°
2,0,2	27.3646°	27.3918°
5,1,1	27.77622°	27.80341°
3,0,2	28.57365°	28.60085°
7,0,1	28.70467°	28.73187°

Mo <sub>4</sub> O <sub>11</sub> Diffraction Peaks		
h,k,l	Observed Peak	Ideal Peak
8,0,0	29.1388°	29.16599°
4,0,2	30.19175°	30.21895°
6,1,1	30.34474°	30.37194°
1,1,2	31.32854°	31.35574°
2,1,2	31.97694°	32.00414°
8,0,1	32.06839°	32.09558°
5,0,2	32.1636°	32.19079°
0,2,0	32.77834°	32.80553°
3,1,2	33.03231°	33.05951°
7,1,1	33.14735°	33.17454°
8,1,0	33.52942°	33.55661°
2,2,0	33.60708°	33.63428°
6,0,2	34.43629°	34.46349°
4,1,2	34.4616°	34.48879°
9,0,1	35.535°	35.5622°
1,2,1	35.6334°	35.6606°
4,2,0	35.99228°	36.01947°
8,1,1	36.14067°	36.16786°
2,2,1	36.21342°	36.24062°
5,1,2	36.22641°	36.25361°
10,0,0	36.66156°	36.68875°
7,0,2	36.96351°	36.99071°
3,2,1	37.16275°	37.18994°
6,1,2	38.28767°	38.31486°

Mo <sub>4</sub> O <sub>11</sub> Diffraction Peaks		
h,k,l	Observed Peak	Ideal Peak
4,2,1	38.45804°	38.48523°
10,0,1	39.09116°	39.11835°
9,1,1	39.29333°	39.32053°
6,2,0	39.69108°	39.71828°
8,0,2	39.7071°	39.7343°
5,2,1	40.07125°	40.09844°
1,0,3	40.19186°	40.21905°
10,1,0	40.33007°	40.35726°
7,1,2	40.60886°	40.63605°
2,0,3	40.71638°	40.74358°
3,0,3	41.57844°	41.60563°
6,2,1	41.97261°	41.9998°
0,2,2	42.55395°	42.58114°
10,1,1	42.58332°	42.61051°
9,0,2	42.63695°	42.66415°
1,2,2	42.72143°	42.74863°
11,0,1	42.72961°	42.75681°
4,0,3	42.76138°	42.78858°
8,1,2	43.15799°	43.18519°
2,2,2	43.22075°	43.24794°
0,1,3	43.44644°	43.47364°
1,1,3	43.61117°	43.63836°
3,2,2	44.04284°	44.07003°
2,1,3	44.1024°	44.1296°

Mo <sub>4</sub> O <sub>11</sub> Diffraction Peaks		
h,k,l	Observed Peak	Ideal Peak
7,2,1	44.13313°	44.16032°
5,0,3	44.24466°	44.27186°
12,0,0	44.35207°	44.37926°
8,2,0	44.43393°	44.46113°
3,1,3	44.91163°	44.93882°
4,2,2	45.17373°	45.20093°
10,0,2	45.73016°	45.75736°
9,1,2	45.90833°	45.93553°
11,1,1	45.99574°	46.02293°
6,0,3	46.00581°	46.033°
4,1,3	46.02571°	46.0529°
12,0,1	46.44731°	46.47451°
8,2,1	46.52629°	46.55348°
5,2,2	46.59602°	46.62321°
5,1,3	47.42818°	47.45537°
12,1,0	47.52996°	47.55715°
7,0,3	48.02218°	48.04937°
6,2,2	48.29038°	48.31758°
10,1,2	48.83844°	48.86564°
11,0,2	48.97°	48.99719°
6,1,3	49.10072°	49.12791°
9,2,1	49.12901°	49.15621°
12,1,1	49.52118°	49.54838°
10,2,0	50.00125°	50.02844°

Mo <sub>4</sub> O <sub>11</sub> Diffraction Peaks		
h,k,l	Observed Peak	Ideal Peak
7,2,2	50.23708°	50.26428°
13,0,1	50.2443°	50.2715°
8,0,3	50.27235°	50.29955°
2,3,0	50.68376°	50.71096°
7,1,3	51.02453°	51.05172°
10,2,1	51.9221°	51.94929°
11,1,2	51.93185°	51.95905°
0,3,1	52.013°	52.04019°
1,3,1	52.15682°	52.18401°
14,0,0	52.25954°	52.28674°
12,0,2	52.34487°	52.37207°
8,2,2	52.41718°	52.44438°
4,3,0	52.42233°	52.44953°
2,3,1	52.58662°	52.61381°
9,0,3	52.73707°	52.76427°
1,2,3	52.80901°	52.8362°
13,1,1	53.15452°	53.18172°
8,1,3	53.18147°	53.20866°
2,2,3	53.23511°	53.26231°
3,3,1	53.29754°	53.32474°
3,2,3	53.94009°	53.96728°
14,0,1	54.12306°	54.15026°
4,3,1	54.28196°	54.30916°
0,0,4	54.29531°	54.32251°

Mo <sub>4</sub> O <sub>11</sub> Diffraction Peaks		
h,k,l	Observed Peak	Ideal Peak
1,0,4	54.43493°	54.46212°
9,2,2	54.81341°	54.8406°
2,0,4	54.85231°	54.87951°
11,2,1	54.89025°	54.91744°
4,2,3	54.91661°	54.9438°
14,1,0	55.09426°	55.12145°
12,1,2	55.17655°	55.20374°
6,3,0	55.23383°	55.26103°
10,0,3	55.39983°	55.42703°
5,3,1	55.5301°	55.5573°
3,0,4	55.54325°	55.57045°
9,1,3	55.55494°	55.58213°
13,0,2	55.8475°	55.8747°
5,2,3	56.15526°	56.18246°
12,2,0	56.24555°	56.27274°
4,0,4	56.50111°	56.5283°
14,1,1	56.89413°	56.92132°
6,3,1	57.03079°	57.05798°
1,1,4	57.19588°	57.22308°
10,2,2	57.41075°	57.43794°
2,1,4	57.59997°	57.62717°
1,3,2	57.63014°	57.65733°
6,2,3	57.64529°	57.67249°
5,0,4	57.71733°	57.74452°

Mo <sub>4</sub> O <sub>11</sub> Diffraction Peaks		
h,k,l	Observed Peak	Ideal Peak
12,2,1	58.02196°	58.04915°
2,3,2	58.0323°	58.05949°
15,0,1	58.08818°	58.11537°
10,1,3	58.13045°	58.15764°
11,0,3	58.24713°	58.27432°
3,1,4	58.26948°	58.29667°
13,1,2	58.56451°	58.59171°
3,3,2	58.69869°	58.72588°
7,3,1	58.7722°	58.79939°
8,3,0	59.01754°	59.04473°
6,0,4	59.18209°	59.20929°
4,1,4	59.19877°	59.22596°
7,2,3	59.37528°	59.40247°
14,0,2	59.47431°	59.50151°
4,3,2	59.62382°	59.65102°
11,2,2	60.19681°	60.22401°
5,1,4	60.38058°	60.40777°
16,0,0	60.445°	60.47219°
15,1,1	60.74133°	60.76853°
8,3,1	60.74258°	60.76978°
5,3,2	60.80061°	60.82781°
7,0,4	60.88498°	60.91218°
11,1,3	60.89601°	60.9232°
12,0,3	61.26857°	61.29577°



Mo <sub>4</sub> O <sub>11</sub> Diffraction Peaks		
h,k,l	Observed Peak	Ideal Peak
13,2,1	61.30929°	61.33649°
8,2,3	61.33388°	61.36107°
6,1,4	61.80652°	61.83371°
14,1,2	62.09131°	62.11851°
16,0,1	62.1462°	62.1734°
6,3,2	62.22088°	62.24808°
8,0,4	62.81559°	62.84279°
9,3,1	62.93091°	62.95811°
16,1,0	63.03812°	63.06531°
14,2,0	63.08631°	63.11351°
12,2,2	63.16201°	63.18921°
15,0,2	63.22497°	63.25217°
7,1,4	63.46766°	63.49485°
9,2,3	63.51043°	63.53763°
10,3,0	63.67415°	63.70135°
12,1,3	63.84232°	63.86952°
7,3,2	63.87593°	63.90312°
13,0,3	64.45691°	64.4841°
16,1,1	64.70018°	64.72737°
14,2,1	64.74769°	64.77489°
0,2,4	64.9021°	64.92929°
9,0,4	64.96413°	64.99133°
1,2,4	65.02734°	65.05454°
10,3,1	65.32738°	65.35458°

Mo <sub>4</sub> O <sub>11</sub> Diffraction Peaks		
h,k,l	Observed Peak	Ideal Peak
8,1,4	65.35507°	65.38227°
2,2,4	65.40233°	65.42953°
15,1,2	65.75583°	65.78303°
8,3,2	65.75703°	65.78422°
10,2,3	65.89545°	65.92264°
0,3,3	65.97387°	66.00107°
3,2,4	66.02484°	66.05204°
1,3,3	66.09806°	66.12526°
13,2,2	66.29964°	66.32683°
17,0,1	66.3057°	66.3329°
2,3,3	66.46991°	66.49711°
4,2,4	66.89135°	66.91855°
13,1,3	66.96291°	66.9901°
3,3,3	67.08736°	67.11455°
16,0,2	67.10219°	67.12938°
10,0,4	67.32192°	67.34912°
9,1,4	67.46037°	67.48756°
14,0,3	67.80796°	67.83516°
9,3,2	67.856°	67.8832°
11,3,1	67.92383°	67.95102°
4,3,3	67.9471°	67.9743°
5,2,4	67.99733°	68.02453°
15,2,1	68.33581°	68.36301°
11,2,3	68.48106°	68.50825°

Mo <sub>4</sub> O <sub>11</sub> Diffraction Peaks		
h,k,l	Observed Peak	Ideal Peak
0,4,0	68.74621°	68.77341°
17,1,1	68.77735°	68.80455°
18,0,0	68.98721°	69.01441°
5,3,3	69.0449°	69.0721°
12,3,0	69.12523°	69.15243°
2,4,0	69.23249°	69.25969°
6,2,4	69.33753°	69.36472°
16,1,2	69.56009°	69.58728°
14,2,2	69.60594°	69.63313°
1,0,5	69.68088°	69.70807°
10,1,4	69.77614°	69.80333°
11,0,4	69.88178°	69.90898°
2,0,5	70.04351°	70.0707°
10,3,2	70.16563°	70.19283°
14,1,3	70.25418°	70.28138°
6,3,3	70.37587°	70.40307°
1,4,1	70.45939°	70.48659°
16,2,0	70.49995°	70.52714°
18,0,1	70.57746°	70.60465°
3,0,5	70.64606°	70.67325°
4,4,0	70.68217°	70.70937°
12,3,1	70.71408°	70.74128°
2,4,1	70.82026°	70.84746°
7,2,4	70.90639°	70.93358°

Mo <sub>4</sub> O <sub>11</sub> Diffraction Peaks		
h,k,l	Observed Peak	Ideal Peak
17,0,2	71.11164°	71.13883°
12,2,3	71.26134°	71.28853°
15,0,3	71.32067°	71.34787°
18,1,0	71.41497°	71.44217°
3,4,1	71.41997°	71.44717°
4,0,5	71.48593°	71.51312°
7,3,3	71.93484°	71.96203°
0,1,5	71.97906°	72.00626°
16,2,1	72.07551°	72.10271°
1,1,5	72.09836°	72.12556°
4,4,1	72.25606°	72.28326°
11,1,4	72.29637°	72.32357°
2,1,5	72.4558°	72.48299°
5,0,5	72.55977°	72.58697°
12,0,4	72.63841°	72.66561°
11,3,2	72.68011°	72.7073°
8,2,4	72.69843°	72.72562°
18,1,1	72.98231°	73.0095°
3,1,5	73.04997°	73.07717°
6,4,0	73.07062°	73.09782°
15,2,2	73.08018°	73.10738°
5,4,1	73.32536°	73.35255°
17,1,2	73.50929°	73.53649°
13,3,1	73.69424°	73.72143°

Mo <sub>4</sub> O <sub>11</sub> Diffraction Peaks		
h,k,l	Observed Peak	Ideal Peak
15,1,3	73.71558°	73.74277°
8,3,3	73.71671°	73.74391°
6,0,5	73.86378°	73.89097°
4,1,5	73.87869°	73.90588°
13,2,3	74.2326°	74.2598°
6,4,1	74.62427°	74.65146°
9,2,4	74.70864°	74.73584°
5,1,5	74.93915°	74.96635°
19,0,1	74.97483°	75.00202°
16,0,3	74.99716°	75.02436°
12,1,4	75.01684°	75.04404°
0,4,2	75.02952°	75.05672°
1,4,2	75.14697°	75.17417°
18,0,2	75.2621°	75.28929°
14,3,0	75.32555°	75.35275°
7,0,5	75.39396°	75.42115°
12,3,2	75.39535°	75.42255°
2,4,2	75.49893°	75.52613°
13,0,4	75.5887°	75.61589°
9,3,3	75.71692°	75.74411°
17,2,1	75.97195°	75.99915°
3,4,2	76.08431°	76.11151°
7,4,1	76.14905°	76.17624°
6,1,5	76.22819°	76.25539°

Mo <sub>4</sub> O <sub>11</sub> Diffraction Peaks		
h,k,l	Observed Peak	Ideal Peak
8,4,0	76.36534°	76.39254°
16,2,2	76.72484°	76.75204°
14,3,1	76.86295°	76.89015°
4,4,2	76.90137°	76.92857°
10,2,4	76.93291°	76.96011°
1,3,4	77.12287°	77.15007°
8,0,5	77.14651°	77.1737°
19,1,1	77.32758°	77.35477°
16,1,3	77.34969°	77.37688°
14,2,3	77.39372°	77.42092°
2,3,4	77.4719°	77.4991°
18,1,2	77.61199°	77.63919°
7,1,5	77.74256°	77.76976°
8,4,1	77.89615°	77.92335°
10,3,3	77.93175°	77.95894°
13,1,4	77.93543°	77.96262°
5,4,2	77.94795°	77.97515°
20,0,0	77.99271°	78.01991°
3,3,4	78.05257°	78.07977°
13,3,2	78.3094°	78.3366°
18,2,0	78.51493°	78.54212°
14,0,4	78.73204°	78.75923°
17,0,3	78.84296°	78.87016°
4,3,4	78.86345°	78.89065°

Mo <sub>4</sub> O <sub>11</sub> Diffraction Peaks		
h,k,l	Observed Peak	Ideal Peak
9,0,5	79.11817°	79.14537°
1,2,5	79.17651°	79.20371°
6,4,2	79.22163°	79.24882°
11,2,4	79.3684°	79.3956°
8,1,5	79.47927°	79.50646°
20,0,1	79.51431°	79.54151°
2,2,5	79.52297°	79.55016°
19,0,2	79.56582°	79.59301°
9,4,1	79.86261°	79.88981°
5,3,4	79.90273°	79.92992°
18,2,1	80.03385°	80.06104°
3,2,5	80.09955°	80.12675°
15,3,1	80.22175°	80.24894°
20,1,0	80.31866°	80.34586°
11,3,3	80.35878°	80.38598°
10,4,0	80.53655°	80.56375°
17,2,2	80.54583°	80.57302°
7,4,2	80.72003°	80.74723°
15,2,3	80.74641°	80.77361°
4,2,5	80.90508°	80.93228°
14,1,4	81.05248°	81.07967°
17,1,3	81.16261°	81.18981°
6,3,4	81.16846°	81.19566°
10,0,5	81.30661°	81.33381°

Mo <sub>4</sub> O <sub>11</sub> Diffraction Peaks		
h,k,l	Observed Peak	Ideal Peak
14,3,2	81.42278°	81.44997°
9,1,5	81.4359°	81.46309°
20,1,1	81.82937°	81.85656°
19,1,2	81.88054°	81.90773°
5,2,5	81.93815°	81.96534°
12,2,4	82.01393°	82.04113°
10,4,1	82.04637°	82.07356°
15,0,4	82.07068°	82.09788°
16,3,0	82.27183°	82.29902°
8,4,2	82.44113°	82.46833°
7,3,4	82.65881°	82.68601°
1,4,3	82.75517°	82.78237°
18,0,3	82.86737°	82.89457°
12,3,3	82.99727°	83.02447°
2,4,3	83.09828°	83.12548°
6,2,5	83.19725°	83.22444°
10,1,5	83.61102°	83.63822°
3,4,3	83.66959°	83.69679°
11,0,5	83.71081°	83.738°
16,3,1	83.77539°	83.80258°
20,0,2	84.03912°	84.06632°
21,0,1	84.2164°	84.2436°
19,2,1	84.27399°	84.30118°
16,2,3	84.29567°	84.32286°



Mo <sub>4</sub> O <sub>11</sub> Diffraction Peaks		
h,k,l	Observed Peak	Ideal Peak
15,1,4	84.37125°	84.39845°
8,3,4	84.37235°	84.39955°
9,4,2	84.38356°	84.41076°
11,4,1	84.44671°	84.47391°
4,4,3	84.46839°	84.49558°
18,2,2	84.55297°	84.58016°
7,2,5	84.6811°	84.7083°
15,3,2	84.7389°	84.7661°
13,2,4	84.87043°	84.89763°
18,1,3	85.16439°	85.19159°
5,4,3	85.49385°	85.52105°
12,4,0	85.56913°	85.59632°
16,0,4	85.61021°	85.63741°
13,3,3	85.84861°	85.8758°
11,1,5	86.00456°	86.03175°
9,3,4	86.30839°	86.33558°
12,0,5	86.33148°	86.35867°
20,1,2	86.33173°	86.35893°
8,2,5	86.38889°	86.41608°
0,0,6	86.40385°	86.43104°
21,1,1	86.50843°	86.53563°
1,0,6	86.51757°	86.54476°
10,4,2	86.54702°	86.57421°
6,4,3	86.74528°	86.77248°

Mo <sub>4</sub> O <sub>11</sub> Diffraction Peaks		
h,k,l	Observed Peak	Ideal Peak
2,0,6	86.85865°	86.88585°
12,4,1	87.06469°	87.09188°
19,0,3	87.0841°	87.1113°
20,2,0	87.21661°	87.24381°
3,0,6	87.42688°	87.45408°
17,3,1	87.53246°	87.55966°
22,0,0	87.61374°	87.64093°
16,1,4	87.89844°	87.92563°
14,2,4	87.94144°	87.96863°
17,2,3	88.05032°	88.07752°
4,0,6	88.22199°	88.24919°
7,4,3	88.22231°	88.2495°
16,3,2	88.26464°	88.29184°
9,2,5	88.32061°	88.34781°
10,3,4	88.46734°	88.49454°
12,1,5	88.61826°	88.64546°
21,0,2	88.7034°	88.7306°
20,2,1	88.71005°	88.73724°
19,2,2	88.76072°	88.78791°
1,1,6	88.80405°	88.83124°
14,3,3	88.9168°	88.94399°
11,4,2	88.93265°	88.95984°
22,0,1	89.10685°	89.13404°
2,1,6	89.14462°	89.17181°

Mo <sub>4</sub> O <sub>11</sub> Diffraction Peaks		
h,k,l	Observed Peak	Ideal Peak
13,0,5	89.17157°	89.19877°
5,0,6	89.24381°	89.27101°
17,0,4	89.36014°	89.38734°
19,1,3	89.36978°	89.39698°
3,1,6	89.71218°	89.73938°
22,1,0	89.89887°	89.92606°
13,4,1	89.90361°	89.93081°
8,4,3	89.92518°	89.95238°